공학박사 학위논문

자기변형 패치 트랜스듀서의 등가 가진 모델을 이용한 유도초음파의 수치해석

Numerical Simulation of Guided Waves using Equivalent Source Model of Magnetostrictive Patch Transducers

2015년 02월

서울대학교 대학원

기계항공공학부

김 화 중

자기변형 패치 트랜스듀서의 등가 가진 모델을 이용한 유도초음파의 수치해석

Numerical Simulation of Guided Waves using Equivalent Source Model of Magnetostrictive Patch Transducers

지도교수 김 윤 영

이 논문을 공학박사 학위논문으로 제출함

2015년 02월

서울대학교 대학원

기계항공공학부

김 화 중

김화중의 공학박사 학위논문을 인준함

2015년 02월

위 원 장 : _____

부위원장 : _____

위　　원 : _____

위　　원 : _____

위　　원 : _____

ABSTRACT

Numerical Simulation of Guided Waves Using Equivalent Source Model of Magnetostrictive Patch Transducers

Hwa Jung Kim
School of Mechanical and Aerospace Engineering
The Graduate School
Seoul National University

While magnetostrictive patch transducers have become more widely used for damage inspection of waveguides such as plates or pipes, the numerical simulation of guided waves excited by the transducers is very limited.

Recently, one-way coupled time-harmonic finite element analysis based on the linearized magnetostrictive coupling equation has been conducted but transient analysis must be carried out for extracting more

information including the reflected waves from cracks. Fully-coupled or one-way coupled multiphysics transient finite element analysis is quite complicated and also requires enormous computational resources.

In order to utilize an advanced structural finite element method or code, we newly propose equivalent distributed force models that can describe the actuation mechanism of the magnetostrictive patch transducer without explicitly solving coupled multiphysics equations. Once equivalent force models are established, transient wave simulations in inspected waveguides can be accomplished efficiently through any structural finite element code.

The essence of this approach is to establish the equivalent actuating force models useful for various types of magnetostrictive patch transducers that are currently available. The validity of the developed models is checked by investigating the wave radiation patterns of the Rayleigh-Lamb and shear-horizontal waves in test waveguides and the simulated results obtained with the proposed models are compared against available experimental results.

Keywords: Magnetostrictive transducer, Equivalent source model, Wave radiation pattern, Transient dynamics finite element analysis

Student Number: 2006-30200

Contents

List of Tables

List of Figures

CHAPTER 1
INTRODUCTION

1.1 Motivation

Guided ultrasonic waves have been widely used for nondestructive evaluation (NDE) in waveguides such as plates and pipes because they can propagate considerable distances along waveguides. To design transducers for NDE in waveguides, one should consider various aspects including wave power, directivity and mode types.

Among various ultrasonic transducers such as magnetostrictive transducers, piezoelectric transducers, and electromagnetic acoustic transducers, this work is mainly focused on ultrasonic wave simulation in a plate or a pipe that is excited by Magnetostrictive Patch Transducers (MPT's). MPT's are based on the magnetostrictive principle that describes the coupling phenomena between magnetic field and elastic deformation.

Because analytical studies of guided waves are usually very limited and complex, finite element simulation has been developed in parallel for the purpose of damage identification. Finite element analysis using equivalent source modeling methods have been widely used in PZT and Electromagnetic Acoustic Transducers (EMATs). Although magnetostriction is phenomenologically analogous to piezomagnetism, little effort has made toward an equivalent source modeling of MPT.

Recently, linearized fully coupled magnetostrictive constitutive

equations using commercial software, COMSOL Multiphysics or time-harmonic finite element analysis using a one-way coupling equation was developed. Some of these analyses could be used directly to simulate time-dependent wave propagation in a waveguide excited by an MPT, but they usually require a large amount of computer resources and enormous amount of CPU time for a coupled multiphysics analysis. Alternatively, we develop an equivalent source modeling method based on a decoupled structural analysis using the finite element modeling technique for efficient finite element simulations involving MPT's.

Hybrid techniques have been introduced to investigate the characteristics of Lamb and shear horizontal wave for the purpose of damage identification, by combining equivalent source modeling methods with finite element simulation, so as to avoid the problems encountered in the sole use of finite element methods.

Thereby, the fully-coupled multiphysics finite element analysis would not be needed and a structural finite element code such as ABAQUS/Explicit can be employed for an efficient analysis of wave propagation phenomena in a waveguide. Equivalent source modeling methods enable to dramatically reduce the CPU time of finite element simulation of MPT's and can be used effectively for design improvement of a wide class of MPT's.

1.2 Research objectives

The objective of this research is to establish the equivalent actuating force models for various types of magnetostrictive patch transducers that are currently developed. An electromagnetic simulation using COMSOL multiphysics analysis capable of predicting the static magnetic field and dynamic magnetic field involved in the electric coil is performed at first step. Simple yet powerful traction force for transient finite element analysis of various types of MPT's is derived and these equivalent forces can replace the actuation by MPT's in transient response finite element simulation. Only transient structural finite element analysis without solving the fully coupled magneto-mechanical equations is performed.

The validity of the developed models is checked by investigating the wave radiation patterns of Rayleigh-Lamb and shear-horizontal waves in test waveguides and simulated results obtained with the proposed models are compared against available experimental results. These hybrid finite element analysis procedures for MPT's can dramatically reduce the CPU time of finite element simulation of Rayleigh-Lamb and shear-horizontal waves induced by MPT's. A large class of problems involving MPT's can be now efficiently solved.

The main objectives associated with this research can be summarized as follows:

- Simulation and validation of circular MPT

In this investigation, the simulation results on the radiation patterns of guided waves generated by an OPMT (Orientation-adjustable Patch-type Magnetostrictive Transducer) according to changes of relative angle between the static and dynamic magnetic fields are validated by available experimental results (Lee *et al.* (2007)). According to the previous research by Cho *et al.* (2006), it was found that Lamb and SH waves were simultaneously generated and measured by OPMT. This simultaneous generation mechanism of Lamb and SH is also identified by finite element simulation. This investigation using equivalent source modeling provides a fundamental help to understand the performance of the circular MPT including the mode-selectivity and directivity characteristics.

- Simulation and validation of beam-focused SH wave MPT

Finite element simulation procedures based on a two-dimensional distributed line source model is developed. Lee *et al.* (2009) suggested a method of focusing only the non-dispersive guided wave in a desired direction by using a specially-configured planar solenoid array (PSA) instead of the figure-of-eight coil. For accuracy and efficiency of guided wave based inspection, the characteristics of the transducer including suitable mode-selection and directivity are the important issues. Here, the simulation

results on the radiation patterns of Rayleigh-Lamb and shear-horizontal waves according to change of frequency is validated by comparing them with available experimental results, respectively. Specifically, damage inspection of a non-ferromagnetic plate structure with oblique crack is investigated.

- Simulation and validation of shear-horizontal wave based pipe damage inspection by a segmented patch array magnetostrictive transducer

The simulation results of angular profile of undamaged pipe are obtained by using equivalent source modeling of MPT at first and these finite element simulation results are verified by available experiments. As applying the suggested equivalent source modeling methods to multilple-crack detection, the validity of the suggested equivalent source modeling method is demonstrated.

- Axially cracked pipe monitoring using helically propagating shear-horizontal waves

Finite element simulation results of helically propagating shear-horizontal waves generated by a specially-configured magnetostrictive transducer on intact pipes are presented by using an equivalent source modeling at first. Helically-propagating SH waves around a crack in a pipe are also investigated by the present simulation scheme.

The equivalence source modeling methods provide a building block to improve and enhance the existing MPT for damage inspection for future work.

1.3 Overview of the thesis

This thesis is concerned with the newly-developed equivalent source modeling of magnetostrictive patch transducers (MPT) and the ultrasonic guided-wave inspection applications using the developed hybrid finite element methods in plate and pipe structures. The validity of the finite element simulation using the proposed equivalent source model will be checked against available experimental results

In Chapter 2, the theory on the magnetostriction is explained first. Then guided wave propagation in plate and hollow cylinders based on the elasticity theory is mentioned. Among several wave modes, S_0 and SH_0 in plate are observed in detail while torsional waves and circumferential shear-horizontal waves in hollow cylinder, respectively. We also provide a comprehensive literature reviews on finite element simulation related to MPT's and equivalent source modeling methods

In Chapter 3, finite element simulations of guided waves by a circular MPT using a figure-of-eight coil for arbitrary relative orientations of the static and dynamic magnetic fields are performed and validated against available experimental results; S_0 and SH_0 are mainly

considered. The characteristics of the simulation results are summarized.

In Chapter 4, the phenomena of focusing the non-dispersive guided wave (SH_0) with specially-configured planar solenoid array (PSA) are simulated by using an equivalent source modeling based on a two-dimensional distributed line source model. In the PSA configuration, the dynamic magnetic field which is produced by the solenoid is superimposed on a static magnetic field in the perpendicular direction. Because the PSA configuration can use the merits of both a meander coil and the figure-of-eight coil, the PSA transducer can focus a desired wave mode along a target direction with a higher-power wave. This chapter shows the comparison results of simulation and experimental results obtained with PSA, such as the radiation pattern.

In Chapter 5, an equivalent source modeling for the segmented magnetostrictive patch transducer is proposed. The angular profile of undamaged pipe which presents the circumferential wave energy distribution is obtained by using wave simulations at first and these finite element simulation results are verified by available experimental results. As applying the suggested equivalent source models to multiple circumferential cracks detection, the validity of the suggested method is demonstrated. Simulation results on monitoring of an axially cracked pipe with helically propagating shear-horizontal waves that are generated by a specially-configured magnetostrictive transducer are also presented.

In Chapter 6, the concluding remarks are presented.

CHAPTER 2
THEORETICAL BACKGROUND

2.1 Introduction

First, we will introduce the basic concept of magnetostriction effect which refers to the coupling phenomenon between magnetic field change and mechanical deformation. It is necessary to understand magnetostriction's characteristics since it is the principal operating mechanism of the magnetostrictive patch transducer. Secondly, the equations of motion of guided waves in a plate and hollow cylinder will be presented. Especially the torsional mode and circumferential shear-horizontal mode will be reviewed in detail among several guided wave modes for the further investigations.

2.2 Magnetostrictive patch transducers (MPT)

Among various transducers, magnetostrictive transducers utilizing a thin ferromagnetic patch have been successfully used for guided-wave in plates and pipes because of high-power generation, effectiveness in generating torsional waves, and easy mode-selection properties (Thompson (1978), Murayama (1996), Kwun and Bartels (1998), Murayama (1999), Murayama and Mizutani (2002), Murayama *et al.* (2003), and Ogi *et al.* (2003)).

Magnetostrictive transducers had been applied to only ferromagnetic waveguides since these types of magneto-mechanical coupling effect can't be generated in non-ferromagnetic materials like aluminum. In

order to generate and sense ultrasonic guided waves in the non-ferromagnetic waveguides, thin ferromagnetic patches are bonded onto a waveguide (Kwun *et al.* (2002)). Light *et al.*(2002) bonded a nickel patch to non-ferromagnetic plates. However, their configurations have some shortcomings to be used for general NDE applications.

To overcome these shortcomings a new type MPT was developed by Cho *et al.* (2004) and Kim *et al.* (2011) as illustrated in figure 2.1 and figure 2.2. As shown in figure 2.1 (a), a typical MPT consists of a thin magnetostrictive circular patch bonded onto a plate, a set of bias magnets and an figure-of-eight electric coil. This transducer has unique feature that the main propagation direction of the generated wave could be adjusted only by rotating the figure-of-eight coil. The freely rotated figure-of-eight coil enables the magnetic field strength to orient mainly in desired direction. Consequently, the desired ultrasonic wave modes can be effectively generated and sensed in the designated direction. The developed transducer was called OPMT (Orientation-adjustable Patch-type Magnetostrictive Transducer). To produce high-power wave and improve the directivity or frequency tuning characteristics, Lee *et al.* (2011) propose a meander coil-type as shown figure 2.1 (b).

Figure 2.2 (a) shows a segmented-patch-array magnetostrictive transducer consisting of a set of segmented magnetostrictive patches, meander coils, and permanent magnets. Segmented patches are attached to the surface of pipe in circumference direction and each patch can generate and measure SH (Shear-Horizontal) waves. The magnetostrictive patch transducer developed for helically propagating

SH waves is shown in figure 2.2 (b). It consists of two rectangular magnetostrictive patches that are tightly bonded onto a pipe, a permanent magnet and a figure-of-eight coil (Kim *et al.* (2012)). This study aims to use the structural finite element simulation, not to solve fully or one-way coupled multiphysics equations, to predict ultrasonic waves generated by MPT's shown in figures 2.1 and 2.2.

2.3 Background to research

2.3.1 Literature reviews on finite element simulation of MPT's and equivalent source modeling method

The finite element methods for MPT's have been developed over the years for their application to plate and pipe structures. Let us examine earlier works related to simulations of magnetostrictive transducers. For instance of finite element (FE) analysis dealing with magnetostrictive transducers, Engdahl and Svensson (Yang *et al.*(2006)) predicted the steady-state response of a magnetostrictive rod due to an applied sinusoidal magnetic field by employing a linearized material model. Carman and Mitrovic (1995) proposed a coupled one-dimensional nonlinear finite element (FE) analysis method to predict the deformation of a magnetostrictive rod. Kannan and Dasgupta (1997) used a three-dimensional FE model based on micromechanical considerations to simulate the phenomena of giant magnetostrictive material like Terfenol-D. Perez-Aparicio and Sosa (2004) developed a fully-coupled dynamic three-dimensional FE model with a consideration of dynamic electromagnetic inertia effects and eddy

current losses due to a frequency-dependent magnetic field. Ribichini *et al.* (2010) proposed a comprehensive model for electromagnetic acoustic transducers to solve linearized coupled magnetostrictive constitutive equations using commercial software, COMSOL Multiphysics. Recently, time-harmonic finite element analysis using a one-way coupling equation was developed (Oh *et al.* (2013)). Sun *et al.* (2014) proposed a new method to enhance the excitation efficiency of the magnetostrictive transmitter for pipe inspection using guided waves by optimizing the axial length of the excitation magnetic field. Liu *et al.* (2010) optimized the configurations of magnetostrictive transducers such as permanent magnet distribution and multilayer coil connection to generate and receive the longitudinal guided waves in steel strands. Choi *et al.* (2005) proposed an equivalent circuit model of thin-strip magnetostrictive transducers for guided wave generation in structural parts.

Because the main efforts in this study are put on the development of an equivalent force model replacing the actuation mechanism of MPT's, It is also necessary to review earlier studies related to equivalence source modeling methods. For instance of the equivalent source modeling methods, Giurgiutiu (2003) suggested the simplified point-force method used in analytic modeling of the PZT wafer-type transducer for the steady-state response of Lamb wave. Lu *et al.* (2008) applied both shear force and bending moment to generate the S_0 and A_0 mode simultaneously to simulate the single PZT actuator on the upper surface of the plate. Yang *et al.* (2006) used the equivalent force and moment which can replace the surface-bounded flat PZT disks to efficiently

describe the emission of guided-wave by piezoelectric actuators. For Lamb wave excitation and detection with embedded piezoelectric wafer active sensors (PWAS), a closed-form Fourier transform of the interfacial shear stress between the PWAS and the structure was obtained under the assumption of ideal bonding (Giurgiutiu(2007)). Raghavan *et al.* (2005) presented a formulation for modeling the GW field excited in-plane traction of uniform magnitude along its perimeter of arbitrary shaped surface-boned piezos in isotropic plates. For EMAT, a hybrid finite element model was suggested to simulate the Lamb wave modes in thin plates using a meander line. COMSOL 2D electromagnetic model is developed for calculating the Lorentz force density, which is the driving force for elastic wave generation within the plate. The calculated force at each node in the finite element model is used for generating elastic wave modes in the plate (Dhayalan and Balasubrmaniam (2010)).

2.3.2 Magnetostrictive effect

Magnetostrictive effect refers to the coupling phenomenon between magnetic field and mechanical deformation in ferromagnetic materials. For a Lamb or shear horizontal wave generation and detection, the transducer uses magnetostrictive effect (or Joule) and its inverse effect (or Viallari). The former means that ferromagnetic material is mechanically deformed by an externally applied magnetic field while the material is mechanically deformed when the magnetic induction of the material is changed. In addition to above mentioned magnetostriction, two other effects related to magnetostriction had been

also reported : the Widedmann effect (1966) is that ferromagnetic rod is twisted when a longitudinal and circular magnetic field are applied simultaneously and the Matteucci (or inverse Widedmann) effect is that a helical anisotropy and electromotive force are generated when a ferromagnetic rod is subjected to a torque.

Macroscopically, during the magnetostriction the ferromagnetic material has experienced two distinct processes and its mechanism in each stage can be explained by domain theory. In first stage individual domains are magnetized as nearly parallel to externally induced magnetic fields and domain walls within the material are migrated in response to external magnetic fields without appreciable rotation out of these directions. Second, the rotation of small magnetic domains is occurred, which are randomly oriented when the material is not exposed to a magnetic field. These two mechanisms of domain movement and rotation make small changes in the physical dimensions of ferromagnetic materials. Although there are many mechanisms explaining the reorientation of the domains, the basic ideas are almost same as those illustrated in figure 2.3. For more understanding on magnetostricion, refer to Bozorth(1993).

The magnetostrictive effect occurs only in a ferromagnetic material such as iron, nickel, cobalt, and their alloys. Among these materials, nickel has negative magnetostriction (shortening under magnetic field) while in others such as Fe, the sign depends crystallographic direction (Perez-Aparicio *et al.* (2002)). In this investigation, the pure nickel is used as a magnetostrictive material. Figure 2.4 shows the

magnetostriction curve of nickel. The static magnetic field is supplied by permanent magnets. The static bias magnetic field is necessary to effectively generate and measure ultrasonic guided waves. When the static bias magnetic field is supplied at the maximum slope region of the magnetostriction curve, large deformation can be obtained only by a small given dynamic magnetic field. The nonlinear magnetostrictive behavior, however, can be linearized about an operating point through the application of a bias magnetic field. Therefore, magnetostrictive and inverse magnetostrictive effect can be expressed by the following two linearized equations:

$$\mathbf{S} = \mathbf{s}^{H}\mathbf{T} + \mathbf{d}^{T}\mathbf{H}_{D} \tag{2.1}$$

$$\mathbf{B}_{D} = \mathbf{d} + \boldsymbol{\mu}\mathbf{H}_{D} \tag{2.2}$$

where $\mathbf{T}$ and $\mathbf{S}$ are the tensors of stress and strain, respectively. The symbols $\mathbf{B}_D$ and $\mathbf{H}_D$ are the vectors of magnetic flux density and the dynamic magnetic field strength, respectively. The tensors $\mathbf{s}^H$, $\mathbf{d}$ and $\boldsymbol{\mu}$ stand for elastic compliance under constant $\mathbf{H}$, piezomagnetic coefficient and permeability, respectively.

2.4 Guided wave theory in a plate structure

For the understanding of the mechanics of the guided wave in plate and pipe structures, the development of the equations of motion for plate and pipe structures is briefly reviewed. The analysis of plate and pipe will follow the those of Giurgitiu V (2003) and Gaziz (1959),

respectively.

The vector form of Navier's governing equations of a stress wave in a homogeneous and isotropic elastic body is

$$(\lambda + \mu)\nabla\nabla \cdot \mathbf{u} + \mu\nabla^2\mathbf{u} = \rho\frac{\partial^2\mathbf{u}}{\partial^2 \mathrm{t}} \tag{2.3}$$

where **u** is the displacement field, ρ is the density, λ and μ are the Lamé constants. To obtain a simplified solution for equation (2.3), the displacement field can be expressed via Helmholtz decomposition of a dilatational scalar potential ϕ and an equivoluminal vector potential **Ψ:**

$$\mathbf{u} = \boldsymbol{\nabla}\phi + \nabla \times \boldsymbol{\Psi} \tag{2.4}$$

The general solution of equation (2.3) is defined for an infinite body, and the theoretical solution can be obtained by applying specific boundary conditions. Substituting equation (2.4) into equation (2.3), the scalar and vector wave equations are obtained as

$$\nabla^2\phi = \frac{1}{C_d^2}\frac{\partial^2\phi}{\partial t^2}, \quad C_d^2 = \frac{\lambda + 2\mu}{\rho} \tag{2.5}$$

$$\nabla^2\boldsymbol{\Psi} = \frac{1}{C_s^2}\frac{\partial^2\boldsymbol{\Psi}}{\partial t^2}, \quad C_s^2 = \frac{\mu}{\rho} \tag{2.6}$$

where C_d and C_s denote the dilatational and distortional wave speeds. The general solution of equation (2.5) and (2.6) is

$$\phi = (A_0 \sin\eta_d y + A_1 \cos\eta_d y) e^{i(kx-\omega t)}$$
$$\psi = (B_0 \sin\eta_s y + B_1 \cos\eta_s y) e^{i(kx-\omega t)} \quad (2.7)$$

where k is wavenumber and

$$\eta_d^2 = \frac{\omega^2}{C_d^2} - k^2, \quad \eta_s^2 = \frac{\omega^2}{C_s^2} - k^2 \quad (2.8)$$

The four integration constants A_0, A_1, B_0 and B_1 are to be found from the traction-free boundary conditions. Using the relations between the potential functions and the displacements, we obtain

$$u_x = [(A_1 ik \cos\eta_d y + B_0 \eta_s \cos\eta_s y) + (A_0 ik \sin\eta_d y - B_1 \eta_s \sin\eta_s y)] e^{i(kx-\omega t)} \quad (2.9)$$

$$u_y = [-(A_1 \eta_d \sin\eta_d y + B_1 ik \sin\eta_s y) + (A_0 \eta_d \cos\eta_d y - B_1 ik \cos\eta_s y)] e^{i(kx-\omega t)} \quad (2.10)$$

The terms in equation (2.9) have been separated into two parts, the first corresponding to symmetric motion and the second to antisymmetric motion. The stresses are given by

$$\tau_{yx} = \mu[(-A_1 2ik\eta_d \sin\eta_d y + B_0 (k^2 - \eta_s^2) \sin\eta_s y) + (A_0 2ik cos\eta_d y + B_1 (k^2 - \eta_s^2) \cos\eta_s y)] \quad (2.11)$$

$$\tau_{yy} = \mu[A_1 (k^2 - \eta_s^2) \cos\eta_d y - B_0 2ik\eta_s \cos\eta_s y + A_0 (k^2 - \eta_s^2) \sin\eta_d y + B_1 2ik\eta_s \sin\eta_s y] \quad (2.12)$$

For a thin plate as shown in figure 2.5 (a), one can apply the traction-free ($\sigma_{yy} = \sigma_{xy} = 0$) boundary conditions at the upper and lower surfaces of the plate (y = ±h, where h is half of the plate thickness). The resulting characteristic equation, known as the Rayleigh-Lamb equation, is written as:

$$F(\Omega^2, \zeta^2) = \frac{tan(\pi\eta_d'/2)}{tan(\pi\eta_s'/2)} + \left[\frac{4\zeta^2\eta_s'\eta_d'}{(\zeta^2 - \eta_s'^2)}\right]^{\pm 1} = 0 \qquad (2.13)$$

where +1 corresponds to symmetric modes and -1 corresponds to anti-symmetric modes. In equation (2.13)

$$\Omega = \frac{\omega}{\omega_s}, \omega_s = \frac{\pi C_s}{2h}, \zeta = \frac{2hk}{\pi}$$
$$\eta_s' = \frac{2h\eta_s}{\pi}, \eta_d' = \frac{2h\eta_d}{\pi} \qquad (2.14)$$

The solution of the transcendental equation (2.13) is not straightforward because η_d' and η_s' also depend on k. We can plot the wave-speed dispersion curves of the guided waves by using numerical solution of equation (2.13). Dispersion curves an aluminum plate is given in figure 2.6. The dispersive wave speed depends on the product *fh* between the frequency (*f*) and the half thickness (*h*). This group velocity curve, which is the speed of propagation of a wave, is very informative for long range inspection. In practice, multi-modes makes it complicate to analyze the measured signals due to the interference with each mode. It is necessary to make the signals as simple as possible in order to avoid the interference of multi-modes. Therefore, the simulation and

experiment performed on this investigation is below the frequency-thickness 1.5 MHz mm. In this region only three modes A_0 (the first antisymmetric Lamb wave), S_0 (the first symmetric Lamb), and SH_0 (the first shear horizontal) exist only.

As can be seen in figure 2.6, the SH_0 is not dispersive because its eigenvalue is zero. Phase velocity and group velocity of SH_0 are same as that of bulk shear wave. A non-dispersive wave is very attractive for long range inspection since the waveform of excited SH_0 wave propagates without any distortion. Therefore the SH_0 mode is most preferred for the guided wave based NDE of a plate-like structure. However, the selective generation of the SH waves are somewhat cumbersome in real applications. Therefore, as an alternative, S_0 mode of the Lamb waves can be used, since neither is it dispersive below a few hundred kHz. In this investigation, therefore, SH_0 and S_0 modes will be considered (Cawley and Alleyne (1996), Lowe *et al.* (1998)).

2.5 Guided wave theory in a hollow cylinder

Now consider the conditions under which harmonic waves may propagate in a hollow cylinder as shown in figure 2.5 (b).

$$\nabla \cdot \boldsymbol{\Psi} = F(\mathbf{r}, \mathrm{t}) \tag{2.15}$$

In equation (2.15) F is a function of the coordinate vector $\mathbf{r}$ and the time, which can be chosen arbitrarily due to the gauge invariance of the

field transformation described by equation (2.4). Let the potentials ϕ and $\boldsymbol{\Psi}$ assume as

$$\begin{aligned}\phi &= f(r)\cos n\theta\cos(\omega t+\kappa_z z)\\ \psi_r &= h_r(r)\sin n\theta\sin(\omega t+\kappa_z z)\\ \psi_\theta &= h_\theta(r)\cos n\theta\sin(\omega t+\kappa_z z)\\ \psi_z &= h_z(r)\sin n\theta\cos(\omega t+\kappa_z z)\end{aligned} \tag{2.16}$$

Substituting equation (2.16) into equations (2.5) and (2.6), the four functions can be determined.

$$\begin{aligned}f(r) &= AZ_n(\bar{\alpha}r)+BW_n(\bar{\alpha}r)\\ 2h_1(r) &= (h_r-h_\theta) = 2A_1Z_{n+1}(\bar{\beta}r)+2B_1W_{n+1}(\bar{\beta}r)\\ 2h_2(r) &= (h_r+h_\theta) = 2A_2Z_{n-1}(\bar{\beta}r)+2B_2W_{n-1}(\bar{\beta}r)\\ h_z(r) &= A_zZ_n(\bar{\beta}r)+B_zW_n(\bar{\beta}r)\end{aligned} \tag{2.17}$$

where

$$\begin{aligned}\alpha^2 &= \frac{\omega^2}{C_d^2}-k_z^2\\ \beta^2 &= \frac{\omega^2}{C_s^2}-k_z^2\end{aligned} \tag{2.18}$$

In equation (2.17), *Z* denotes the first kind of Bessel function *J* or modified Bessel function *I*, and *W* denotes the second kind of Bessel function *Y* or modified Bessel function *K*, according to Table 2.1. The

arguments $\bar{\alpha}r = |\alpha r|$ and $\bar{\beta}r = |\beta r|$, depending on whether α and β, as determined by equation (2.18), are real or imaginary.

The property of gauge invariance is used to eliminate two of the integration constants of equations (2.17). Owing to this property, any one of the three potentials h_1, h_2, h_z may be set to zero without loss of the generality of solution. Physically, this implies that the displacement field corresponding to an equivoluminal potential of equations (2.17) can also be derived by a combination of the other two equivoluminal potentials. The resulting displacement fields are then given by

$$u_r = \left[f' + \frac{n}{r}h_z + k_z h_1\right] \cos n\theta \cos(\omega t + \kappa_z z) \tag{2.19}$$

$$u_\theta = \left[-\frac{n}{r}f + k_z h_1 - h_z'\right] \sin n\theta \cos(\omega t + \kappa_z z) \tag{2.20}$$

$$u_z = \left[-k_z f - h_1' - (n+1)\frac{h_1}{r}\right] \cos n\theta \sin(\omega t + \kappa_z z) \tag{2.21}$$

Where primes denote differentiation with respect to r, strain components are derived from strain-displacement. And the stress fields can be obtained by Hook's law,

$$\sigma_{ij} = \lambda(\varepsilon_{rr} + \varepsilon_{\theta\theta} + \varepsilon_{zz})\delta_{ij} + 2\mu\varepsilon_{ij} \tag{2.22}$$

The resulting stress fields are

$$\sigma_{rr} = \left[-\lambda(\alpha^2 + k_z^2)f + 2\mu\left\{f'' + \frac{n}{r}\left(h_z' - \frac{h_z}{r}\right) + k_z h_1'\right\}\right]$$

$$\times \cos n\theta \cos(\omega t + \kappa_z z) \quad (2.23)$$

$$\sigma_{r\theta} = \mu\left[-\frac{2n}{r}\left(f' - \frac{f}{r}\right) - k_z\left(\frac{n+1}{r}h_1 - h_1'\right)\right.$$
$$\left.-(2h_z'' - \beta^2 h_z)\right] \times \sin n\theta \cos(\omega t + \kappa_z z) \quad (2.24)$$

$$\sigma_{rz} = \mu\left[-2k_z f' - \frac{n}{r}\left\{h_1' + \left(\frac{n+1}{r} - (\beta^2 - k_z^2)\frac{r}{n}\right)h_1\right\}\right.$$
$$\left.-\frac{n}{r}k_z h_z\right] \times \cos n\theta \sin(\omega t + \kappa_z z) \quad (2.25)$$

Since the hollow cylinder has an inner radius *a* and outer radius *b*, with cylindrical coordinates as shown in figure. 2.5 (b), we impose the traction-free boundary conditions at inner and outer surfaces of a hollow cylinder

$$\sigma_{rr} = \sigma_{r\theta} = \sigma_{rz} = 0 \; at \; r = a, b \quad (2.26)$$

Substituting stress fields into equation (2.26) yields characteristics equation, formed by the determinant of the coefficients of amplitudes A, B, A_1, B_1, A_z, and B_z.

$$\left|C_{ij}\right| = 0, i, j = 1,2, \ldots 6 \quad (2.27)$$

For nontrivial solution, the system determinant must vanish. There are numerous torsional, longitudinal, and flexural modes propagating in a

hollow cylinder axially. And they are labeled $\mathrm{L}(0,n), \mathrm{T}(0,n)$, and $\mathrm{F}(n,m)$ $(n,m = 1,2,\dots)$, respectively((see Gazis (1959) and Achenbach (1975)).

2.5.1 Torsional mode in a hollow cylinder

Since main concerns of this research in pipe are the guided torsional wave, the only torsional mode will be derived. The torsional modes are assumed to contain only u_θ component of the particle displacement and propagating in the z-axis direction. In the expressions for the displacement components, the displacements for n = 0 correspond to the axisymmetric modes. Setting $f = h_1 = 0$ in equations (2.19), (2.20), and (2.21), one can obtain the motion involving displacements u_θ only. Thus remaining displacement and stress fields are

$$u_\theta = -h_z' \cos(\omega t + k_z z) \tag{2.28}$$

$$\sigma_{r\theta} = -\mu(2h_z'' + \beta^2 h_z)\cos(\omega t + k_z z) \tag{2.29}$$

The traction-free condition is imposed at inner and outer surfaces of a hollow cylinder. Thus, one arrives at a linear system of two homogeneous equations in two unknowns. It may be ascertained that no roots exist for the torsional waves if $\beta^2 < 0$. Thus the phase velocity of the torsional waves is always greater than or equal to C_s. For a nontrivial solution of equation, the system determinant must be vanish, yielding the following frequency equation,

$$J_2(\beta a)Y_2(\beta b) - J_2(\beta b)Y_2(\beta a) = 0 \tag{2.30}$$

Using equation (2.30), the dispersion relation of the torsional wave can be obtained. The dispersion relations in terms of the frequency-wave number and the frequency-group velocity calculated from equation (2.30) are shown in figure 2.7. From the figure, one can see that the fundamental torsional wave T(0,1) is completely non-dispersive at all frequencies while other higher modes are dispersive. Recently, most practical testing has been done with the fundamental torsional mode because the shape of the pulse of fundamental torsional mode is not distorted during propagation. And another attractive property of fundamental torsional wave is that it is not affected by higher modes if the excitation frequency is lower than the first cut-off frequency (the cut-off frequency of the second branch).

2.5.2 Circumferential Shear-Horizontal mode in a hollow cylinder

To understand wave propagation in a curved surface of a hollow cylinder, one should know dispersion characteristics of waves propagating in a circumferential direction of a hollow cylinder. In this section, only the circumferential SH (Shear-Horizontal) wave will be considered. For more discussions on guided circumferential waves, see Qu *et al.* (1996) and Zhao and Rose (2004).

Among the displacement components, consider only the displacement in the *z* direction, that is,

$$u_r = u_\theta = 0,\ u_z \neq 0 \tag{2.31}$$

and the motion is independent of axial coordinate *z*, Now consider the conditions under which harmonic waves may propagate along the θ direction in a hollow cylinder. Then, the displacement field u_z can be assumed as

$$u_z = \Gamma(r)e^{i(kb\theta-\omega t)},\ \mathrm{a} \leq \mathrm{r} \leq \mathrm{b} \tag{2.32}$$

where, for convenience, the wave number *k* is defined by

$$\mathrm{k} = \frac{\omega}{C(b)} \tag{2.33}$$

In equation (2.32), $C(r)$ is the linear phase velocity for material particles located a distance *r* from the *z*-axis of the hollow cylinder. Substituting equation (2.33) into equation (2.3) yields

$$\Gamma'' + \frac{1}{r}\Gamma' + \left[\left(\frac{\omega}{C}\right)^2 - \left(\frac{kb}{r}\right)^2\right]\Gamma = 0 \tag{2.34}$$

Here, primes denote differentiation with respect to *r*. Now introduce the nondimensional variables used in Zhao and Rose (2004)

$$\bar{r} = \frac{r}{b}, \bar{k} = kh, h = b - a$$
$$\hat{k} = kb, \hat{\omega} = \frac{\omega b}{c_s}, \eta = \frac{a}{b} \tag{2.35}$$

The solution of equation (2.34) can be written as

$$\Gamma(r) = AJ_{\hat{k}}(\hat{\omega}\bar{r}) + BY_{\hat{k}}(\hat{\omega}\bar{r}),\ \text{a} \le \text{r} \le \text{b} \tag{2.36}$$

where $J_{\hat{k}}$ and $Y_{\hat{k}}$ are the first and second kind of Bessel functions of order $\hat{k}$. And *A* and *B* are arbitrary constants. From equation (2.32), u_z can be rewritten as

$$u_z(r) = [AJ_{\hat{k}}(\hat{\omega}\bar{r}) + BY_{\hat{k}}(\hat{\omega}\bar{r})]e^{i(kb\theta - \omega t)},\ a \le r \le b \tag{2.37}$$

The traction free condition is imposed at inner and outer surfaces of a hollow cylinder. Thus, one arrives at a linear system of two homogeneous equations in two unknowns. For a nontrivial solution of equation, the system determinant must be vanish, yielding the following frequency equation,

$$\begin{aligned}&[J_{\hat{k}-1}(k_T a) - J_{\hat{k}+1}(k_T a)][Y_{\hat{k}-1}(k_T b) - Y_{\hat{k}+1}(k_T b)]\\ &-[J_{\hat{k}-1}(k_T b) - J_{\hat{k}+1}(k_T b)][Y_{\hat{k}-1}(k_T a) - Y_{\hat{k}+1}(k_T a)]\end{aligned} \tag{2.38}$$

where $k_T = \omega/c_s$ is the wave number of the shear wave. Using equation (2.38), the dispersion relation of the circumferential SH wave can be obtained. Figure 2.8 shows the dispersion relations in terms of curves

calculated from equation (2.38) for two hollow cylinders with different outer diameters and the same thickness. From the figure, one can see that dispersive characteristics of the lowest branch of the circumferential SH wave is unlike those of the SH_0 wave in a flat plate. The dispersive characteristics of SH wave of hollow cylinder are much affected by larger curvature of cylinder than smaller one.

Table 2.1 Bessel functions used at different intervals of the frequency ω

Interval	Functions used
$c_d k_z < \omega$	$J(\alpha r)$, $Y(\alpha r)$, $J(\beta r)$, $Y(\beta r)$
$c_s k_z < \omega < c_d k_z$	$I(\bar{\alpha} r)$, $K(\bar{\alpha} r)$, $J(\beta r)$, $Y(\beta r)$
$\omega < c_s k_z$	$I(\bar{\alpha} r)$, $K(\bar{\alpha} r)$, $I(\bar{\beta} r)$, $K(\bar{\beta} r)$

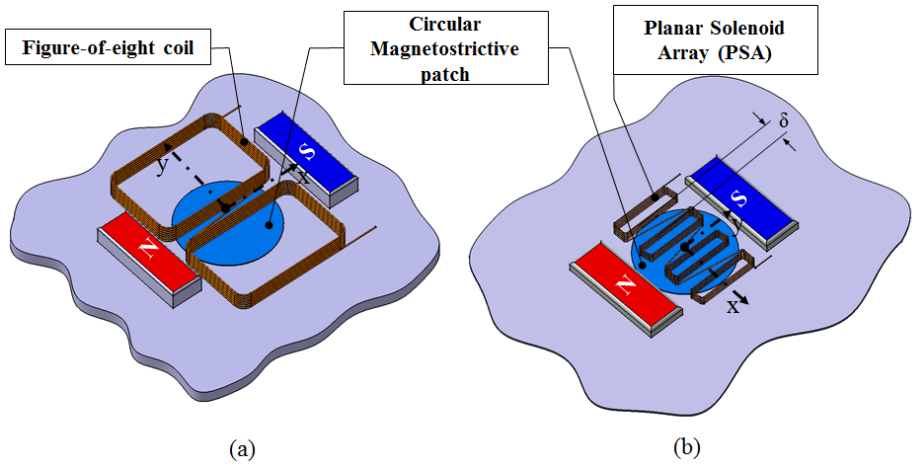

Figure 2.1 Magnetostrictive patch transducers using (a) a figure-of-eight coil (Lee *et al.* (2007)) and (b) a planar solenoid array coil (Lee *et al.* (2011)). (In actual configuration $\delta \cong 0$). Note that the transducers in (a) and (b) are called an OPMT (Orientation-adjusted Patch-type Transducer) and a PSA-OPMT (PSA : Planar Solenoid Array).

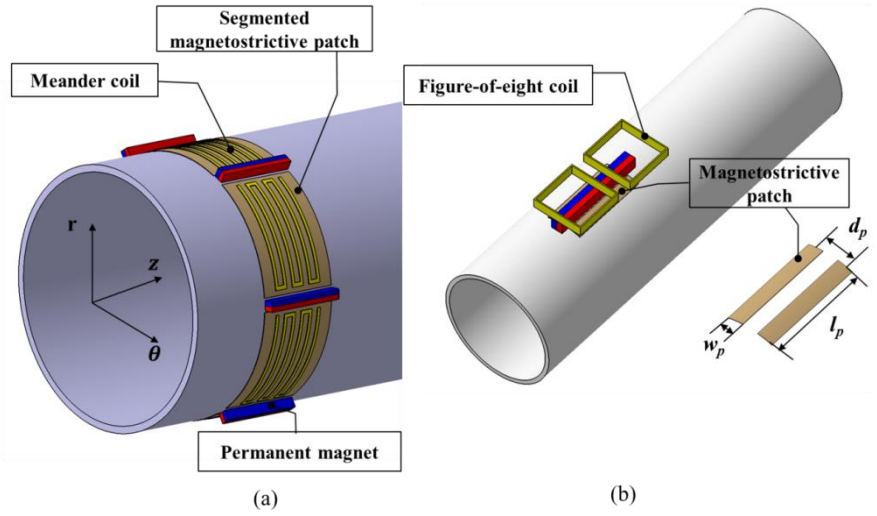

Figure 2.2 (a) A segmented-patch-array magnetostrictive transducer installed on a pipe (Kim *et al.* (2011)) and (b) a magnetostrictive transducer designed to generate frequency-tuned helically propagating shear-horizontal waves (Kim *et al.* (2012)).

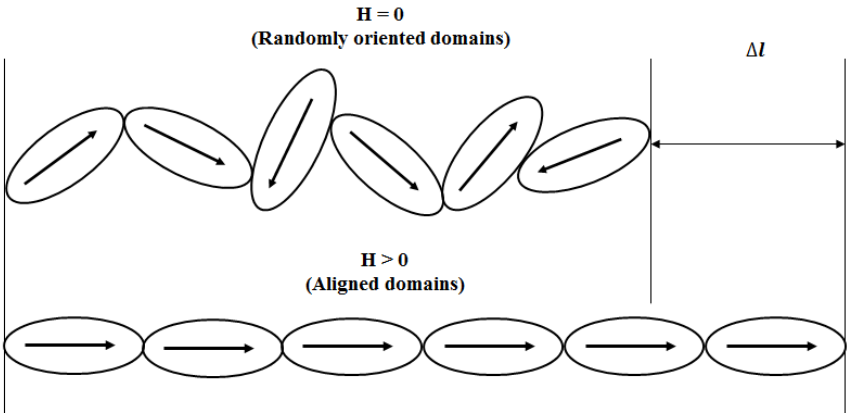

Figure 2.3 Physical length change in a ferromagnetic material caused by the rotation and movement of magnetic domains.

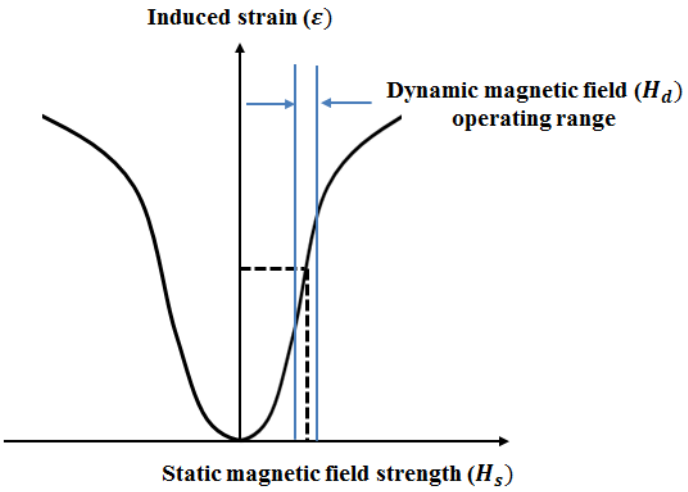

Figure 2.4 An magnetostrictive curve representing the relation between the magnetic field strength H and strain ε.

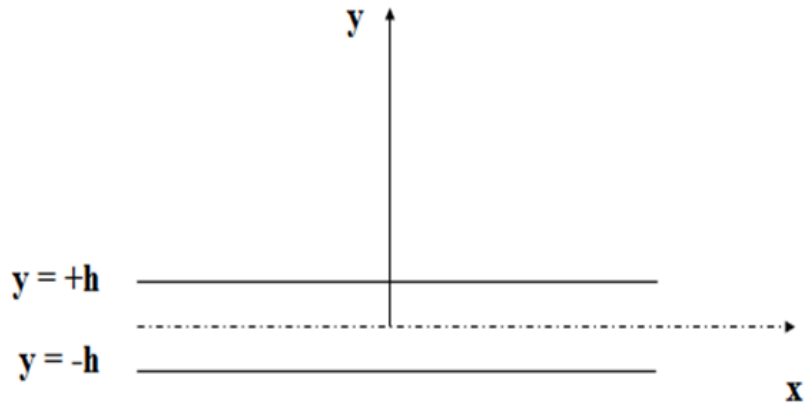

(a)

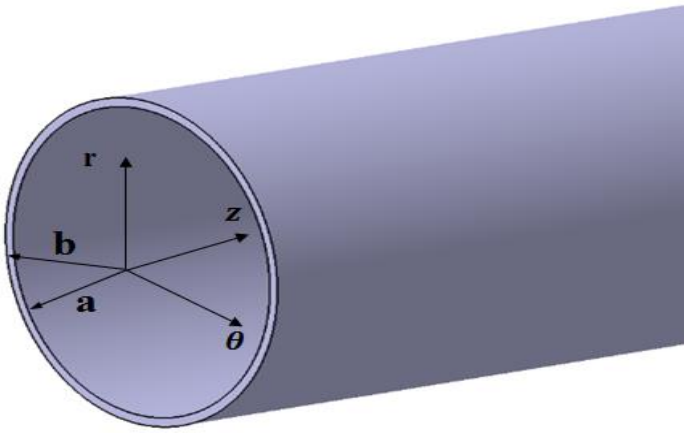

(b)

Figure 2.5 (a) Coordinates of the free plat with thickness 2h and (b) coordinates for an infinitely long hollow circular cylinder.

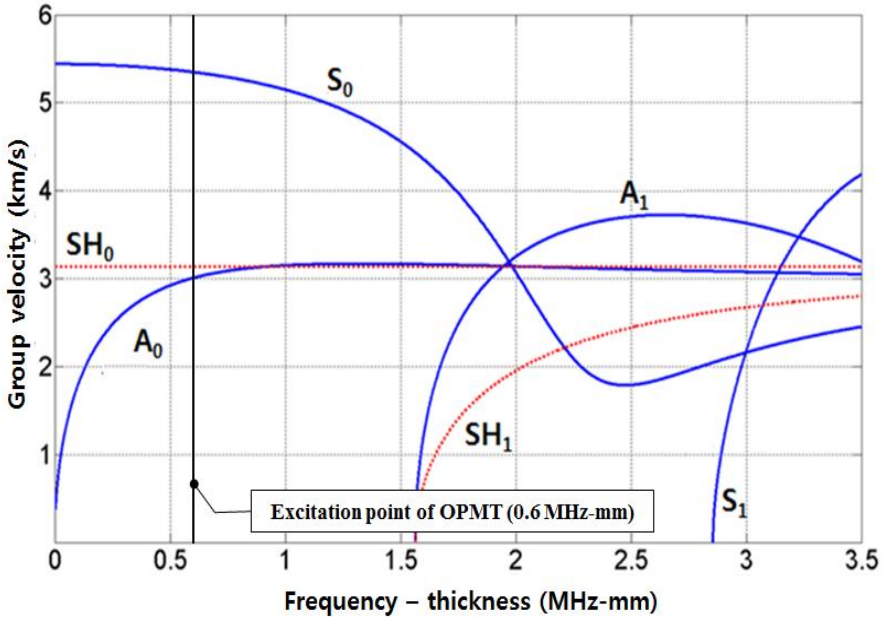

Figure 2.6 The dispersion curve for an aluminum plate.

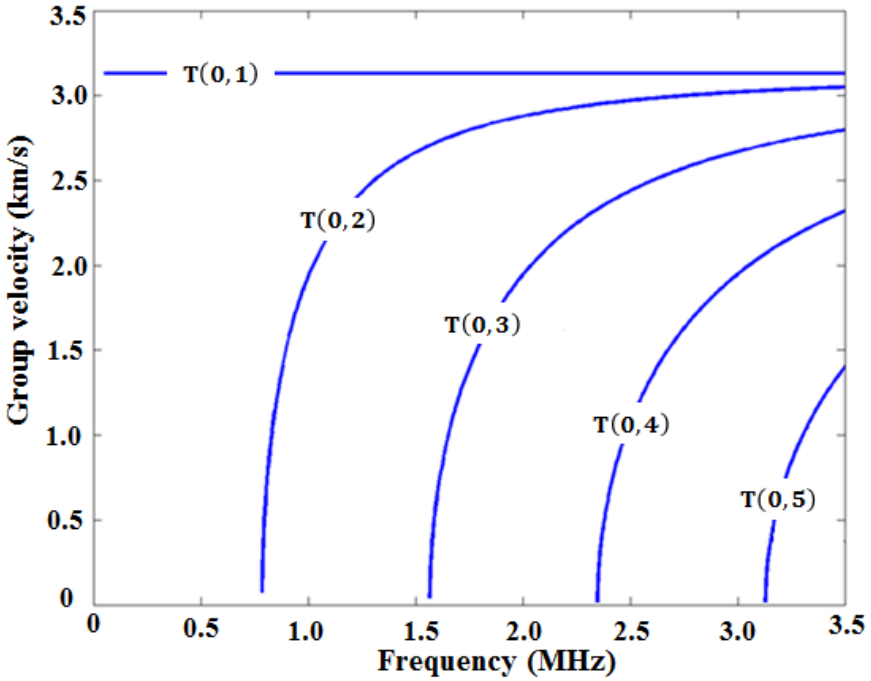

Figure 2.7 The dispersion curve for the torsional wave in a hollow aluminum cylinder with an outer diameter of 25 mm and a thickness of 2 mm.

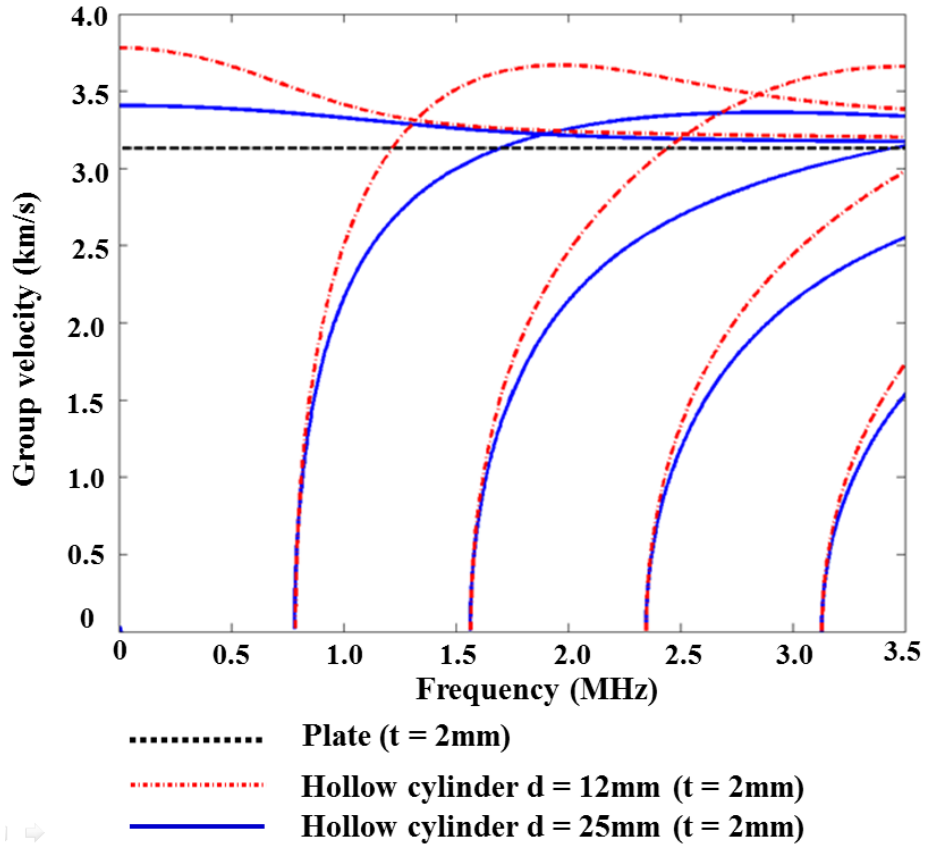

Figure 2.8 The dispersion curve for circumferential SH waves in hollow aluminum cylinders.

CHAPTER 3
GUIDED WAVE TRANSDUCTION IN A CIRCULAR MPT USING A FIGURE-OF-EIGHT COIL BY AN ARBITRARY-ANGLED STATIC BIASING MAGNETIC FIELD

3.1 Introduction

This chapter is concerned with finite element simulations on the radiation pattern of Lamb and Shear Horizontal (SH) waves generated by a circular magnetostrictive patch transducer (MPT) using a figure-of-eight coil with varying θ from 0° to 90° with increment of 15°, which means relative orientations of both static basing magnetic field and dynamic actuating magnetic field.

To facilitate analysis and also to better demonstrate the present method, we will consider non-ferromagnetic test plates as considered in (Lee *et al.* (2007 and 2009)). In developing equivalent force models, the understanding of the nonlinear magnetostrictive phenomenon is essential from which a linearized relation between input current and actuating distributed forces will be derived. Definitely, a static bias magnetic field induced by a set of permanent magnets as shown in figure 3.1 should be properly considered for the derivation. The static field deforms the magnetostrictive patch by a certain amount and a dynamic magnetic field of a small magnitude is superposed to the patch to generate dynamic deformation in the patch. The latter field is

generated by a current flown into electrical coils located above the magnetostrictive patch. Figure-of-eight coils in figure 3.1 (a) will be considered. Once the dynamic magnetic field is applied, the patch will be dynamically deformed and its deformation can be treated to be linear. Since the magnetostrictive patch is bonded onto a waveguide, the deformation of patch generates force (or stress) in the waveguide. It is known (Thompson (1997 and 1978)) that the Lamb waves are generated if the static bias field is parallel to the dynamic field while the SH waves are generated if the static field is perpendicular to the dynamic field.

Because the patch is firmly bonded onto a waveguide, there must be interactions between the patch and the waveguide. The distributions of the force applied to the plate by an MPT can be calculated by the one-way linearized piezomagnetic constitutive equations as long as the magnetic field in the patch can be assumed to be uniform (Oh *et al.* (2013)). Thereby, the fully-coupled multiphysics finite element analysis would not be needed and a structural finite element code such as ABAQUS/Explicit can be employed for an efficient analysis of wave propagation phenomena in a waveguide. When an MPT is used as a receiver, a model similar to the transmitter mentioned above can be constructed if necessary.

The MPT shown in figure 3.1 is usually referred to as the OPMT (Orientation-adjustable Patch-type Magnetostrictive Transducer) and the abbreviation will be used here. They consists of i) magnetostrictive

patches bonded onto a plate, ii) permanent magnets providing static bias magnetic field to the patches and iii) electric coils providing dynamic actuation magnetic field to the patches. When an MPT is used as an actuator, the deformation of the magnetostrictive patch resulting from the magneto-mechanical coupling effect of the patch subject to dynamic magnetic field generates elastic waves in a plate. On the other hand, the coil senses magnetic field change in the patch when an MPT is used as a receiver. If a plate is assumed to be excited by an external source, wave propagation in a plate can be analyzed by purely-structural finite element analysis using shells or elastic bodies.

3.2 Experimental setup

Experiments of radiation pattern of the Lamb and SH waves for arbitrary values of θ were conducted by Lee *et al.* (2007) and these available experiment results were used as reference data for simulation results. Experiment procedures are briefly introduced for more accurate understanding. The figure 3.2 shows the experimental setup. The thickness of aluminum plate is 2 mm. The diameter and thickness of nickel patches in OPMT's are 10mm and 0.15mm, respectively. Scotch-Weld Epoxy DP-460 was used as a bonding material. The symbol α in figure 3.2 denotes the relative angle between the x-axis and the line connecting from the transmitter patch center to the receiver patch center. We will consider various different angles between the dynamic magnetic field ($\mathbf{H}_D$) and the static field ($\mathbf{H}_S$). Because wave phenomena

in a plate will be investigated in this study, it will be useful to plot the dispersion relations in a plate. Figure 2.6 shows the dispersion curves in a test aluminum plate where the symbols S_n and A_n denote the *n*th branches of the symmetric and anti-symmetric Rayleigh-Lamb modes while SH_n, the *n*th branch of the shear-horizontal mode. The excitation frequency of 300 kHz (corresponding to the frequency-thickness product of 0.6 MHz-mm) is below the cutoff frequencies of the S_1 and SH_1 modes and there are only the first symmetric Lamb wave mode (S_0) and the first shear-horizontal wave mode (SH_0).

The transducer consists of two antisymmetrically polarized permanent magnets for a biasing magnetic field and a figure-of-eight coil for an actuating dynamic magnetic field. The bobbin holding a figure-of-eight coil can rotate freely relative to the housing of the permanent magnets. As illustrated in figure 3.2, the direction of static magnetic field ($\mathbf{H_S}$) is fixed along the horizontal *x* axis while the direction of dynamic magnetic field ($\mathbf{H}_D$) can be varied. The symbol α denotes the wave propagation direction from the transducer at the origin ($x=0$, $y=0$) to a sensor located r = 200 mm. The sensors can selectively measure either Lamb wave or SH wave by just rotating the permanent magnets; for measuring Lamb waves, a circular MPT with $\theta=0^\circ$ was used. In case of measuring SH waves, a circular MPT with $\theta=90^\circ$ was used. For experiments, sensors were located at every 15° of α for a given value of θ.

3.3 Equivalent Source Modeling of OPMT

To develop an equivalent force model to replace an actuating MPT, it is necessary to investigate how elastic waves are generated by MPT's. When a circular nickel patch bonded to a test plate is subjected to both a static biasing magnetic field by two magnets and a dynamic actuating magnetic field by a coil, the patch deformation by magnetostriction generates guided waves in the plate. Earlier studies (Cho *et al.* (2007)) show that if the OPMT's in figure 3.1 (a) are used, both the Lamb waves and SH waves are simultaneously generated. This is closely related to the magnetic field distributions formed in the magnetostrictive patch as shown in figure 3.3 (a). Because two coils with same current direction are placed over the center of nickel patch, the dynamic magnetic field is distributed over the whole area of nickel patch (Lee *et al.* (2007)) as shown in figure 3.3 (a). The directions of static magnetic field of OPMT are same as x-axis.

As explained in introduction, the dynamic field is parallel with (or perpendicular to) the static field, the Lamb wave (or the SH wave) alone will be generated in the plate. Because the dynamic strain field is mainly responsible for wave generation in a plate through mechanical deformation in a patch, we will be mainly focused on the dynamic field as force sources. In the presence of a bias static magnetic flux, the dynamic magnetic field generates the traction forces within the nickel patch according to equation (2.1). Equations (2.1) show that the strain field and dynamic magnetic field affect bilaterally, and thus represent

two-ways fully-coupled equations. However, a one-way coupling equation which can simplify the complicated analysis can be used because the generation of magnetic field by stress may be neglected for the analysis of MPT's (Oh *et al.* (2013)). So, the following form of one-way coupling equations can be employed:

$$\mathbf{S} = \mathbf{s}^{\mathrm{H}}\mathbf{T} + \mathbf{S}_{\mathrm{MS}} \tag{3-1}$$

$$\mathbf{B}_{\mathrm{D}} = \boldsymbol{\mu}^{\mathrm{T}}\mathbf{H}_{\mathrm{D}} \tag{3-2}$$

where $\mathbf{S}_{\mathrm{MS}}$ is an additional excitation strain due to the magnetostriction effect, which is defined as (Oh *et al.* (2013))

$$\mathbf{S}_{\mathrm{MS}} = \mathbf{d}^{\mathrm{T}}\mathbf{H}_{\mathrm{D}} \tag{3.3}$$

An equivalent source modeling method, which is similar to the point-force model replacing the actuation by PZT (Giurgiutiu (2003), Lu *et al.* (2008), Yang *et al.* (2006) and Raghavan *et al.* (2005)) and EMAT (Dhayalan *et al.*(2010), Murayama *et al.* (1996)) is adopted to simulate the MPT's. The derivation of the resulting traction force distribution on the aluminum plate is the key in this analysis. Once the forces are determined, they will be used as the driving forces in purely-structural finite element analysis. Note that the dynamic magnetic fields are generated through the coils into which an alternating electric current is flown.

Let us consider the OPMT case and develop an equivalent force model. In figure 3.4 (a), the static biasing field $\mathbf{H}_S$ and dynamic actuating field $\mathbf{H}_D$ are simultaneously applied to excite the nickel patch. The $\mathbf{H}_D$ field can be divided into H_x, H_y and H_z. If the direction of static magnetic field $\mathbf{H}_S$ is uniform in the *x* direction on the entire surface of the nickel patch, the only non-vanishing terms **d** will be d_{11}, d_{12} and d_{35}. Therefore, non-zero strain components (with $H_z \cong 0$) will be written as

$$\begin{Bmatrix} \varepsilon_{xx}^{NP} \\ \varepsilon_{yy}^{NP} \\ \varepsilon_{xy}^{NP} \end{Bmatrix} = \begin{bmatrix} d_{11} & 0 & 0 \\ d_{12} & 0 & 0 \\ 0 & d_{35} & 0 \end{bmatrix} \begin{Bmatrix} H_x \\ H_y \\ H_z \end{Bmatrix} \tag{3.4}$$

The superscript *NP* stands for "Nickel Patch," while we will use a superscript *AP* to denote "Aluminum plate." The components of **d** (d_{11}, d_{12}, d_{35}) in equation (3.4) are defined as (see, e.g. Oh *et al.* (2013))

$$\begin{aligned} d_{11} &= \left.\frac{\partial f(H)}{\partial H}\right|_{H_S} \\ d_{12} &= -\frac{d_{11}}{2} \\ d_{35} &= 3\left.\frac{f(H)}{H_S}\right|_{H_S} \end{aligned} \tag{3.5}$$

where $f(H) \equiv \mathrm{S}$ is strain developed in the patch under a unidirectional magnetic field H. The magnitude of the static field is

denoted by $H_S = |\mathbf{H}_S|$. The dynamic field $\mathbf{H}_D$ was assumed to be approximately uniform and planar. If ideal bonding between the aluminum plate and nickel patch is assumed, the continuity in the in-plane (*x*-*y*) strain components between the surface layer of the aluminum plate and the OPMT disk can be expressed as

$$\varepsilon_{xx}^{AP} = \varepsilon_{xx}^{NP}, \varepsilon_{yy}^{AP} = \varepsilon_{yy}^{NP}, \varepsilon_{xy}^{AP} = \varepsilon_{xy}^{NP} \tag{3.6}$$

Using the stress-strain relation in an aluminum plate

$$\begin{Bmatrix} \sigma_{xx}^{AP} \\ \sigma_{yy}^{AP} \\ \sigma_{xy}^{AP} \end{Bmatrix} = \begin{bmatrix} \frac{E}{(1-\nu^2)} & \frac{E\nu}{(1-\nu^2)} & 0 \\ \frac{E\nu}{(1-\nu^2)} & \frac{E}{(1-\nu^2)} & 0 \\ 0 & 0 & \frac{E}{2(1+\nu)} \end{bmatrix} \begin{Bmatrix} \varepsilon_{xx}^{AP} \\ \varepsilon_{yy}^{AP} \\ \varepsilon_{xy}^{AP} \end{Bmatrix} \tag{3.7}$$

where E and ν are Young's modulus and Poisson's ratio of the aluminum plate. Substituting equations (3.4) to (3.5) into equation (3.7) yields

$$\begin{aligned} \sigma_{xx}^{AP} &= \frac{E d_{11}}{(1-\nu^2)} \left(\frac{2-\nu}{2}\right) H_x \\ \sigma_{yy}^{AP} &= \frac{E d_{11}}{(1-\nu^2)} \left(\frac{2\nu-1}{2}\right) H_x \\ \sigma_{xy}^{AP} &= \frac{E}{2(1+\nu)} d_{35} H_y \end{aligned} \tag{3.8}$$

If the *x*-axis is parallel to the direction of the static field $\mathbf{H}_S$, the

relations in equation (3.8) clearly show how stresses in the aluminum plate are generated. For future development, let us write H_x and H_y as $H_x = H_D\cos\theta$, $H_y = H_D\sin\theta$ where is defined in figure 3.4 (a). Then, equations (3.8) are re-written as

$$\begin{aligned}
\sigma_{xx}^{AP} &= \frac{Ed_{11}}{(1-\nu^2)}\left(\frac{2-\nu}{2}\right)H_D\cos\theta \\
\sigma_{yy}^{AP} &= \frac{Ed_{11}}{(1-\nu^2)}\left(\frac{2\nu-1}{2}\right)H_D\cos\theta \\
\sigma_{xy}^{AP} &= \frac{E}{2(1+\nu)}d_{35}H_D\sin\theta
\end{aligned} \tag{3.9}$$

The developed stress field given by equations (3.9) can be treated as the field generated by a distributed force along the circumference of a circle of the magnetostrictive patch radius *a* as

$$\begin{aligned}
\boldsymbol{q} &= q_x\boldsymbol{e_x} + q_y\boldsymbol{e_y} \\
&= c\boldsymbol{n}\cdot\boldsymbol{\sigma}^{AP}|_{at\ r=a} \\
&= c\boldsymbol{e_r}\cdot\sigma_{ij}^{AP}\boldsymbol{e_i}\otimes\boldsymbol{e_j}\ \ (i,j=1,2) \\
&= c\left(\boldsymbol{e_x}\cos\gamma + \boldsymbol{e_y}\sin\gamma\right)\cdot\sigma_{ij}^{AP}\boldsymbol{e_i}\otimes\boldsymbol{e_j}
\end{aligned} \tag{3.10}$$

where *c* is a scaling or calibration constant and $\boldsymbol{e_i}$ is the unit based vector along the *i*th coordinate. The definition of the angle γ is illustrated in figure 3.4. From (3.10), one can find

$$q_x = c(\sigma_{xx}^{AP}\cos\gamma + \sigma_{xy}^{AP}\sin\gamma)$$
$$q_y = c(\sigma_{xy}^{AP}\cos\gamma + \sigma_{yy}^{AP}\sin\gamma) \tag{3.11}$$

Substituting equation (3.9) into (3.11), with the definition of $\zeta = \frac{f(H)}{H_s}\Big/\frac{\partial f(H)}{\partial H}\Big|_{H_s}$, yields

$$q_x = \frac{cEd_{11}H_D}{(1-\nu^2)}\left(\frac{(2-\nu)}{2}\cos\theta\cos\gamma + \zeta\frac{3(1-\nu)}{2}\sin\theta\sin\gamma\right)$$
$$q_y = \frac{cEd_{11}H_D}{(1-\nu^2)}\left(\zeta\frac{3(1-\nu)}{2}\sin\theta\cos\gamma + \frac{(2\nu-1)}{2}\cos\theta\sin\gamma\right) \tag{3.12}$$

The magnetostriction curve of the nickel patch interpolated by a hyperbolic tangent function (Oh *et al.* (2013)) with the value of the static magnetic field H_S calculated at the edge of the nickel patch obtained from magnetic analysis (e.g, by using COMSOL) is used to evaluate ζ. (For the problems considered in this study, the calculated value ζ was $\zeta = 0.67$.) Figure 3.4 (c) shows the distributions of $\boldsymbol{q}$ for the angle between H_D and H_S equal to 0°, 45° and 90°, respectively.

3.4 Finite Element Simulation and Verification

The finite element based wave simulation is performed with a commercial code, ABAQUS/Explicit using the equivalent force model developed in the previous section. The time increment scheme in

ABAQUS/Explicit is automatically adjusted, so no user input is necessary. Following the numerical stability limit, the discretization parameters in time and space are chosen from

$$\Delta t \leq \frac{min(\Delta x, \Delta y, \Delta z)}{C_d} \tag{3.13}$$

where C_d is the dilatational wave speed and $(\Delta x, \Delta y, \Delta z)$ denote the smallest mesh sizes in the *x*, *y*, and *z* coordinates. The mesh sizes in a finite element model should be determined by the smallest wavelength λ_{min} to be considered. If n_{min} is the minimum number of nodes per wavelength and C_{min} is the group velocity corresponding to λ_{min}, the following condition (Yang *et al.* (2006)) is used for satisfactory solution convergence (for a two-dimensional finite element model) :

$$n_{min} = \frac{\lambda_{min}}{\max(\Delta x, \Delta y)} = \frac{C_{min}}{\max(\Delta x, \Delta y) f} \tag{3.14}$$

In the present analysis, n_{min} is chosen to be 17 for the Lamb wave and 10 for the SH wave by taking the nominal element length $(\Delta x, \Delta y)$ to be 1 mm. These values are found to be small enough to capture the S_0 and SH waves accurately. An aluminum plate to which OPMT's are

installed is discretized by plane stress elements (CPS4R) of ABAQUS/Explicit. The plates considered in this study have the dimension of 900 mm × 900 mm × 2 mm and are made of aluminum (see Table 3.1 for the material properties). Figure 3.5 (a) shows the locations of the actuating and sensing OPMT's bonded onto a test plate. The actuation mechanism by the actuating OPMT is replaced by a set of equivalent forces prescribed on the circular boundary of the OPMT patch, as indicated in figure 3.5 (b). The applied force distribution follows equation (3.12) while the time dependence of the force $f_{GP}(t)$ (*t*: time) is given by

$$f_{Gp}(t) = \frac{\cos(\eta t)}{(\pi\hat{\sigma})^{\frac{1}{4}}} e^{-\frac{t^2}{2\hat{\sigma}^2}} \tag{3.15}$$

where η is the center frequency and $\hat{\sigma}$ is a parameter to control the spread of the pulse over time. To compare the present numerical results with experimental results conducted earlier (Lee *et al.* (2007)), we chose $\eta = 300$ kHz, r_s (distance between the actuating OPMT and the sensing OPMT's) = 200 mm and α (measurement angle) = 15°.

3.4.1 Analysis of Wave Radiation Pattern in a Plate Excited by OPMT's

Let us now explain how to determine the wave radiation pattern for each mode from simulated results of a transient structural finite element

analysis in which the developed equivalent force models are employed. The stress amplitude-time histories are extracted for all measurement points that are arranged on a circle centered at the location of the actuating MPT. These data are normalized with respect their maximum value in order to plot the wave radiation pattern by an MPT. Figure 2.6 shows that modes generated at this actuation frequency are S_0 and SH_0 marked in figure 2.6. To distinguish the Lamb and SH waves from the FE analysis results, we examine the normal stress (σ_{rr}) and shear stress ($\sigma_{r\theta}$) components, respectively. Table 3.2 shows that the wave group velocities by the FE simulation agree favorably with the theoretical and experimental (Lee *et al.*(2007)) results. The snapshots of wave motion at *t* (time) = 6.0E-05 sec are shown in figure 3.6. As identified with S_0 and SH_0 in figure 3.6, the examination of σ_{rr} and $\sigma_{r\theta}$ alone is sufficient enough to identify the wave modes generated by OPMT's. It is obvious from this figure that the peak-to-peak values of S_0 and SH_0 vary depending on the relative angle θ between the static biasing and dynamic actuating magnetic fields. Figure 3.7 shows that the present simulation results by the proposed equivalent force model are in close agreement with the experimentally measured values (Lee *et al.* (2007)). For $\theta = 0^{\circ}$, the largest amplitude of the S_0 mode wave appears at $\alpha = 0^{\circ}$ (and 180°) and that of SH_0 mode, at $\alpha = \pm 45^{\circ}$. When $\theta = 45^{\circ}$, the largest amplitude of the S_0 wave appears around $\alpha = 26^{\circ}$, which compares well with the experimental result $\alpha = 25^{\circ}$ (experiments were taken at every 15°(Lee $et\ al.(2007)$). The present simulation also predicts that the

largest SH_0 wave appears at $\alpha = 70^{\circ}$. Figure 3.6(c) predicts that the largest magnitude of the S_0 wave appears at $\alpha = \pm 45^{\circ}$, which is that same angle found in experiments (Lee *et al.* (2007)).

The numerical and experiment results of OPMT can be summarized as follows:

1) In case of static biasing field $\mathbf{H}_S$ is parallel to dynamic actuating field $\mathbf{H}_D$ ($\theta = 0^{\circ}$), the directions of the static and dynamic magnetic fields are exactly same as x axis ($\alpha = 0^{\circ}$). If we assume that wave generation with MTP's with small-sized nickel patch acts like the wave generation by a point source. The stress components at a point of nickel patch is obtained from equation (3.9) by applying ($\theta = 0^{\circ}$) as

$$\sigma_{xx}^{AP} = \frac{E d_{11}}{(1-\nu^2)}\left(\frac{2-\nu}{2}\right) H_D$$
$$\sigma_{yy}^{AP} = \frac{E d_{11}}{(1-\nu^2)}\left(\frac{2-\nu}{2}\right) H_D \qquad (3.16)$$
$$\tau_{xy}^{AP} = 0$$

It is especially of interest to find the orientation planes where maximum normal stress and maximum shear stress act upon because S_0 and SH_0 waves propagate along these principle axes, respectively. Because Mohr's circle shows the stress components on any other plane with a

different orientation passing through that point, it can be used effectively to find the direction of principal stress and maximum shear stress. As shown in figure 3.11 (a), the largest shear stress is occurred along the direction making an angle of $\alpha = \pm 45^0$ with x-axis. In Mohr's circle there are major principal stress and minor principal stress. The major elongation and contraction deformation of the patch is developed along major principal axis. S_0 has maximum value along $\alpha = 0^{\circ} (\alpha = 180^{\circ})$. Another S_0 wave out of phase due to Poisson's effect propagates along minor principal axis. These predictions using More's circle are consistent with those of experiment and transient dynamic analysis of OPMT. In transient dynamic analysis, the phase of S_0 becomes reversed after passing $\alpha = 60^{\circ}$ and $\alpha = 120^{\circ}$, and no S_0 mode is generated at $\alpha = 60^{\circ} (\alpha = 240^{\circ})$ and $\alpha = 120^{\circ} (\alpha = 300^{\circ})$.

2) Similar arguments also apply in case of static biasing field $\mathbf{H}_S$ is perpendicular to dynamic actuating field $\mathbf{H}_D$ $H_B (\theta = 90^{\circ})$, The stress components at a point of nickel patch is obtained from equation (3.9) by applying $(\theta = 90^{\circ})$ as

$$\sigma_{xx}^{AP} = \sigma_{yy}^{AP} = 0;\ \tau_{xy}^{AP} = \frac{E d_{35}}{2(1+\nu)} H_D \qquad (3.17)$$

It is a pure shear stress state as shown figure 3.11 (c). The largest shear stress is occurred along with x-axis and y-axis respectively. The major principal and minor principal axis is occurred along the direction

making an angle of $\alpha = \pm 45^{\circ}$ with x-axis. The maximum value of S_0 is found along $\alpha = 45^{\circ}(\alpha = 225^{\circ})$ and $\alpha = 135^{\circ}(\alpha = 315^{\circ})$. No S_0 wave is generated along $\alpha = 0^{\circ}(\alpha = 180^{\circ})$ and $\alpha = 90^{\circ}(\alpha = 270^{\circ})$.

3) In case of wave generation by an MPT with $\theta = 45^{\circ}$, The stress components at a point of nickel patch is obtained from equation (3.9) by applying($\theta = 45^{0}$) as

$$\sigma_{xx}^{AP} = \frac{E d_{11}}{\sqrt{2}(1-\nu^2)}\left(\frac{2-\nu}{2}\right) H_D$$
$$\sigma_{yy}^{AP} = \frac{E d_{11}}{\sqrt{2}(1-\nu^2)}\left(\frac{2\nu-1}{2}\right) H_D \qquad (3.18)$$
$$\tau_{xy}^{AP} = \frac{E d_{35}}{2\sqrt{2}(1+\nu)} H_D$$

The orientation of the planes where the maximum and minimum principal stress act can be determined by the following equation as shown figure 3.11 (b)

$$tan2\theta_p = \frac{2\sigma_{xy}^{AP}}{\sigma_{xx}^{AP} - \sigma_{yy}^{AP}} = 2\zeta \qquad (3.19)$$

The direction of major principal axis and maximum shear stress is occurred at $\theta_p = 26.6^{\circ}$ ($\theta_p = 26.6^{\circ} + 180^{\circ}$) and $\theta_p = 71.6^{\circ}$ ($\theta_p = 71.6^{\circ} + 180^{\circ}$). These results can explain why S_0 and SH_0 waves

propagates along around $\alpha = 25^{\circ}$ and $\alpha = 70^{\circ}$ in experiment, respectively.

3) At angles of θ between 0° and 90°, the direction of the maximum magnitude line rotates counterclockwise as θ increases.

5) For a given θ, the magnitude of SH_0 is the same when the wave signal is measured at α, $\alpha + 90^{\circ}$, $\alpha + 180^{\circ}$, and $\alpha + 270^{\circ}$ while the pulses measured at α and $\alpha + 90^{\circ}$ are out of phase with each other. This is due to the characteristics of shear deformation and the circular shape of the patch.

6) No shear wave is measured at 45° off from the radiation direction of the maximum SH_0 directions.

Figure 3.9, 3.10 and 3.11 show radiation patterns of S_0 and SH_0 wave for varying θ.

3.5 Summary

The radiation pattern of the guided waves generated by a circular nickel patch was investigated by finite element simulations with equivalent source modeling. The simultaneous generation mechanism of Lamb and SH wave is explained by traction forces distributions of aluminum plate. The radiation patterns of S_0 and SH_0 resembles a four-leaved

clover shape and rotates counterclockwise as θ increases from $\theta = 0°$ to $\theta = 90°$. The comparison of the experimental results (Lee *et al*. (2007)) and finite element simulation results shows that the developed equivalent source modeling method accurately predicts the radiation patterns of the S_0 and SH_0 waves and obtained its adequacy .

Table 3.1 Mechanical properties of aluminum alloy plates

Thickness *h* (mm)	**Young's modulus *E* (GPa)**	**Poisson's ratio ν**	**Density ρ ($\mathbf{kg}/m^3$)**
2	71	0.33	2.7×10^3

Table 3.2 Comparison of simulation and experimental results of wave group velocities at 300 kHz

Lamb wave mode	FE simulation (m/sec)	Experiment (m/sec)	Theory (m/sec)
S_0	5281	5210	5222
SH_0	3046	3085	3130

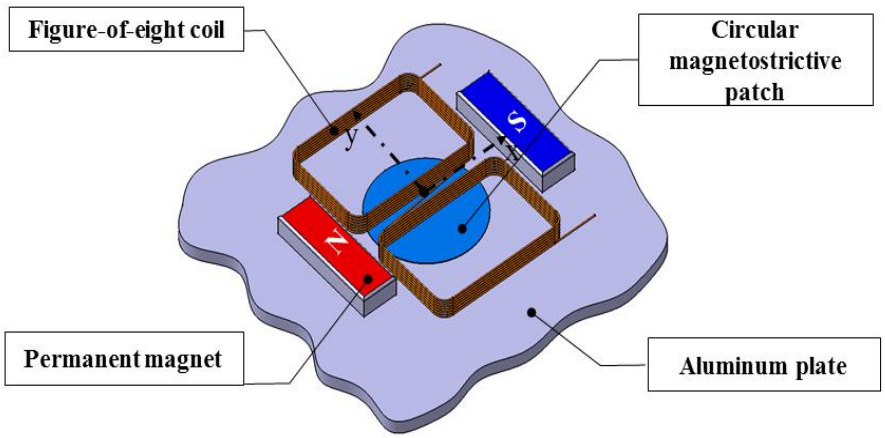

(a)

Figure 3.1 Magnetostrictive patch transducers using a figure-of-eight coil (Lee *et al.*(2007)) Note that the transducers is called an OPMT (Orientation-adjusted Patch-type Transducer).

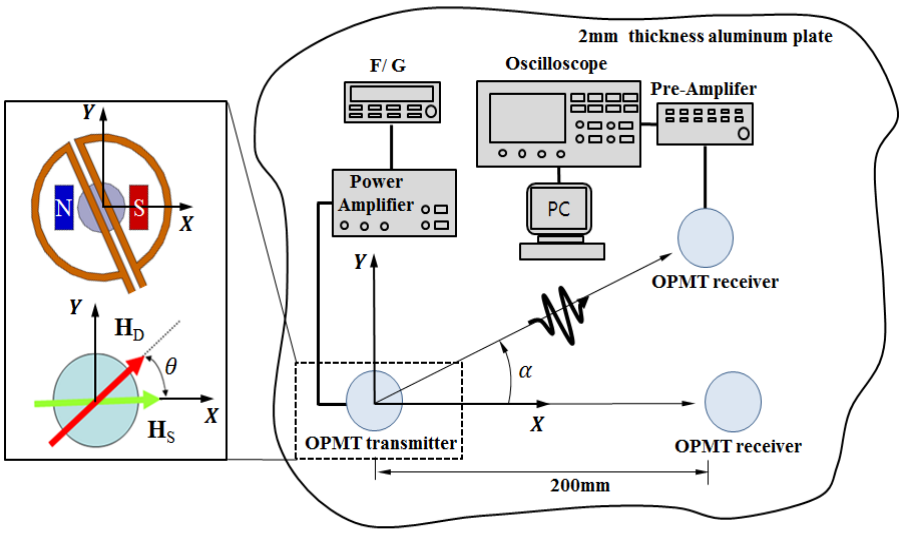

Figure 3.2 Experimental setup in a aluminum plate by using OPMT's or PSA-OPMT's.

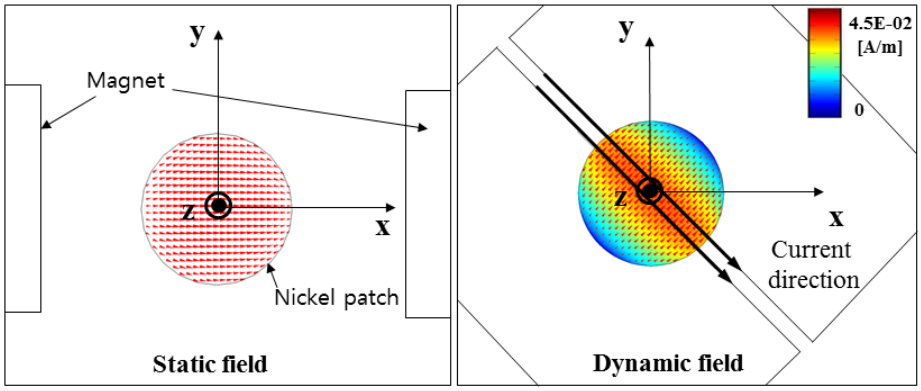

Figure 3.3 (a) The static and (b) dynamic magnetic field distributions induced by a figure-of-eight coil.

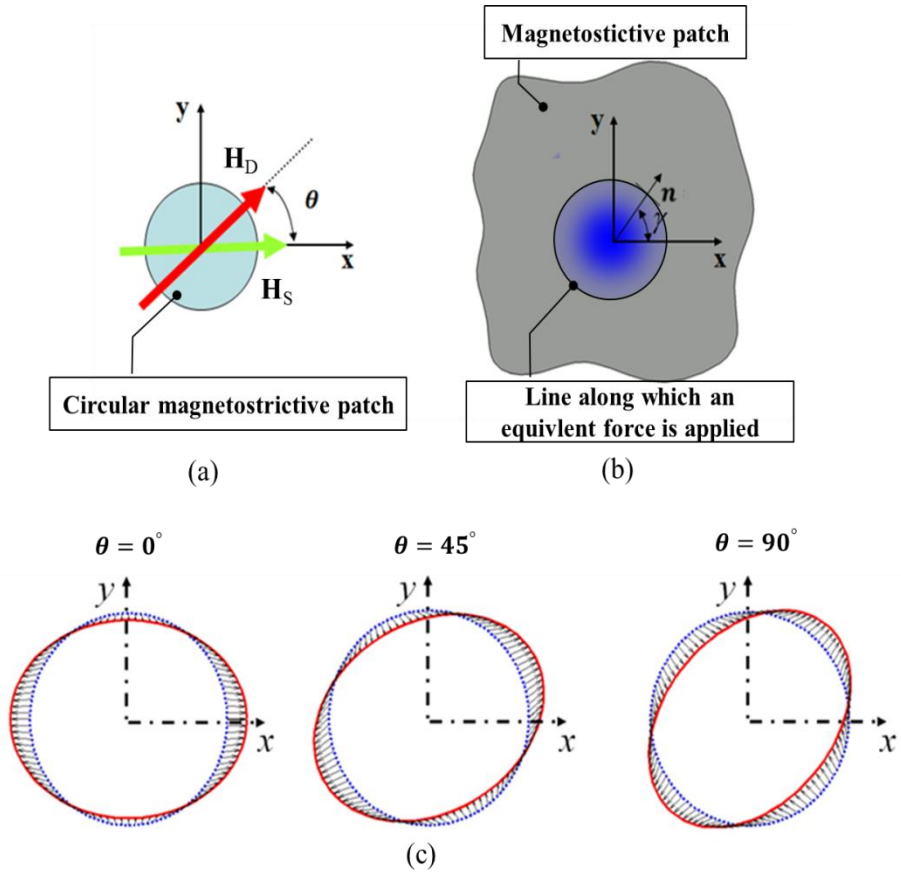

Figure 3.4 (a) Directions of static ($\mathbf{H}_S$) and dynamic ($\mathbf{H}_D$) magnetic fields applied on a magnetostrictive patch of an MPT, (b) The line along which an equivalent distributed force is applied and the unit vector $\boldsymbol{n}$ normal to the line and (c) the distribution of $\mathbf{q}$ for different values of θ (the angle between $\mathbf{H}_D$ and $\mathbf{H}_S$).

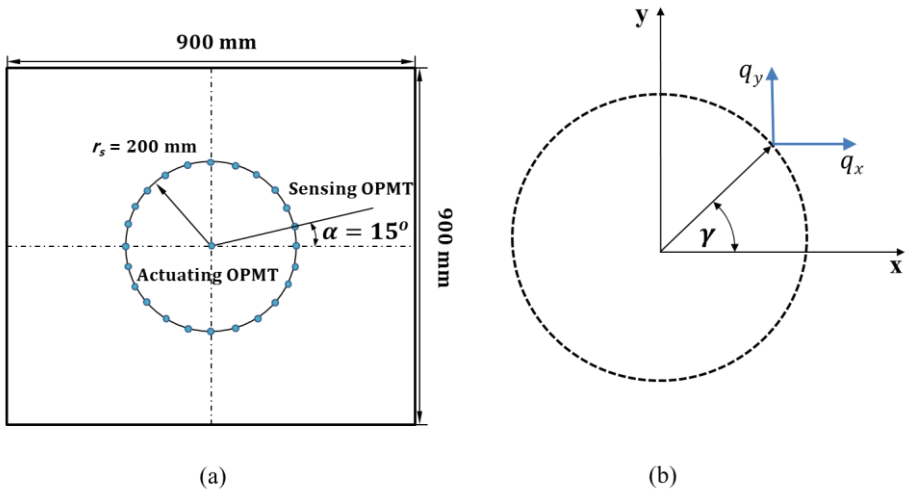

(a) (b)

Figure 3.5 (a) The locations of the actuating and sensing OPMT's installed on a test aluminum pipe and (b) the equivalent force prescribed on the circular boundary of the OPMT patch.

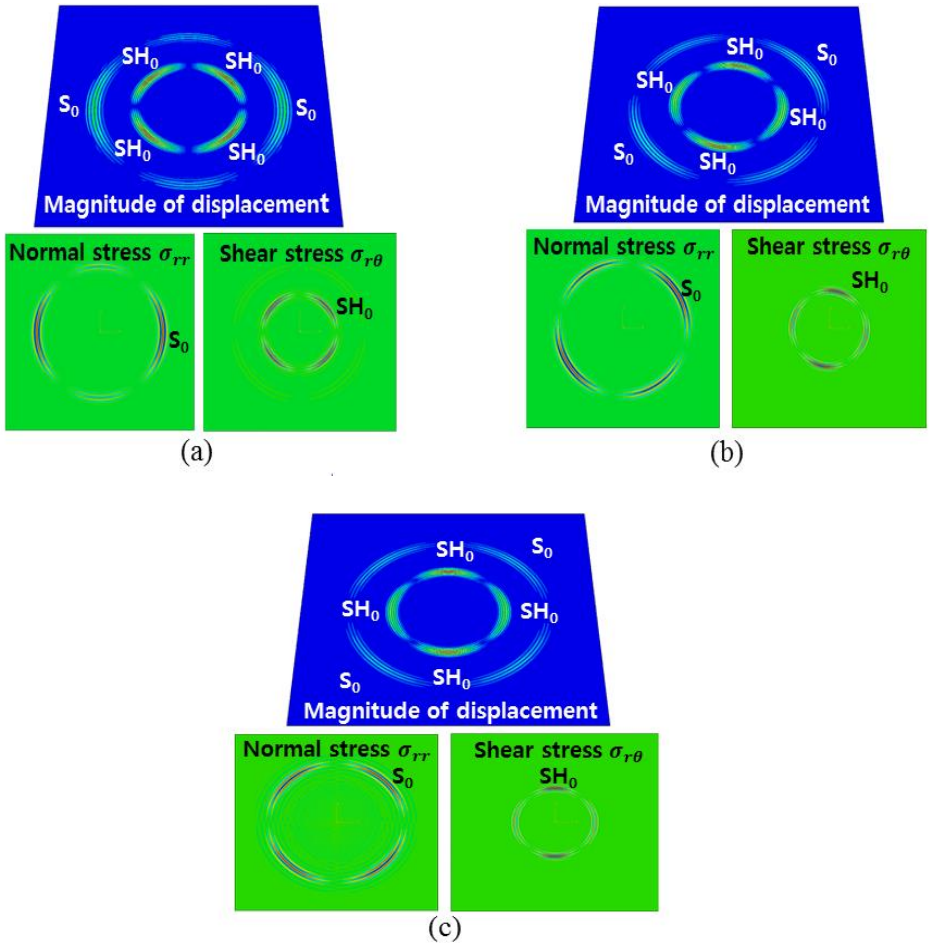

Figure 3.6 Snapshots of the magnitude of the displacement and stress (σ_{rr} and $\sigma_{r\theta}$) in a plate excited by an OPMT at η = 300 kHz (time = 6.0E-05s). The angle (θ) between $\mathbf{H}_D$ and $\mathbf{H}_S$ is (a) 0°, (b) 45° and (c) 90°.

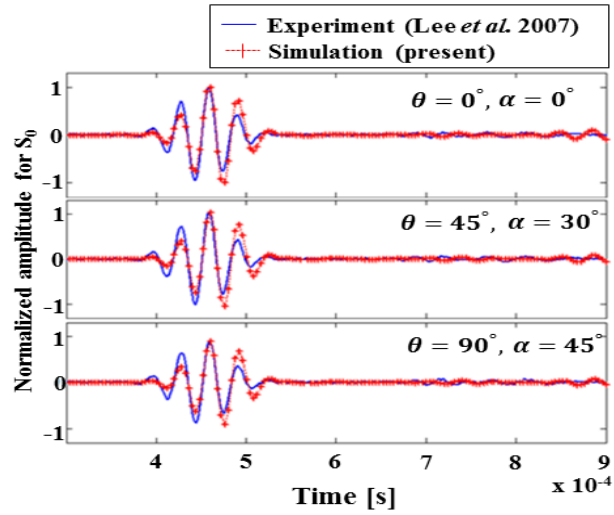

(a)

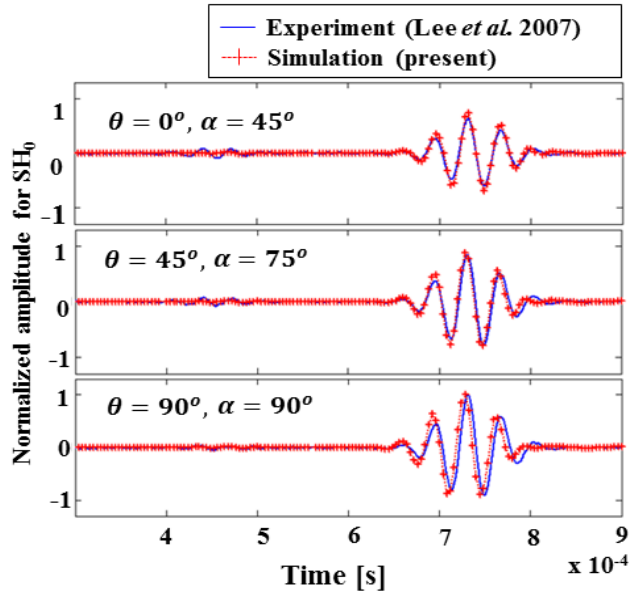

(b)

Figure 3.7 The time histories of the wave signals by PSA-OPMT's for (a) $\alpha = 0^{\circ}$, 30°, 45° and (b) $\alpha = 45^{\circ}$, 75°, 90° with varying θ values.

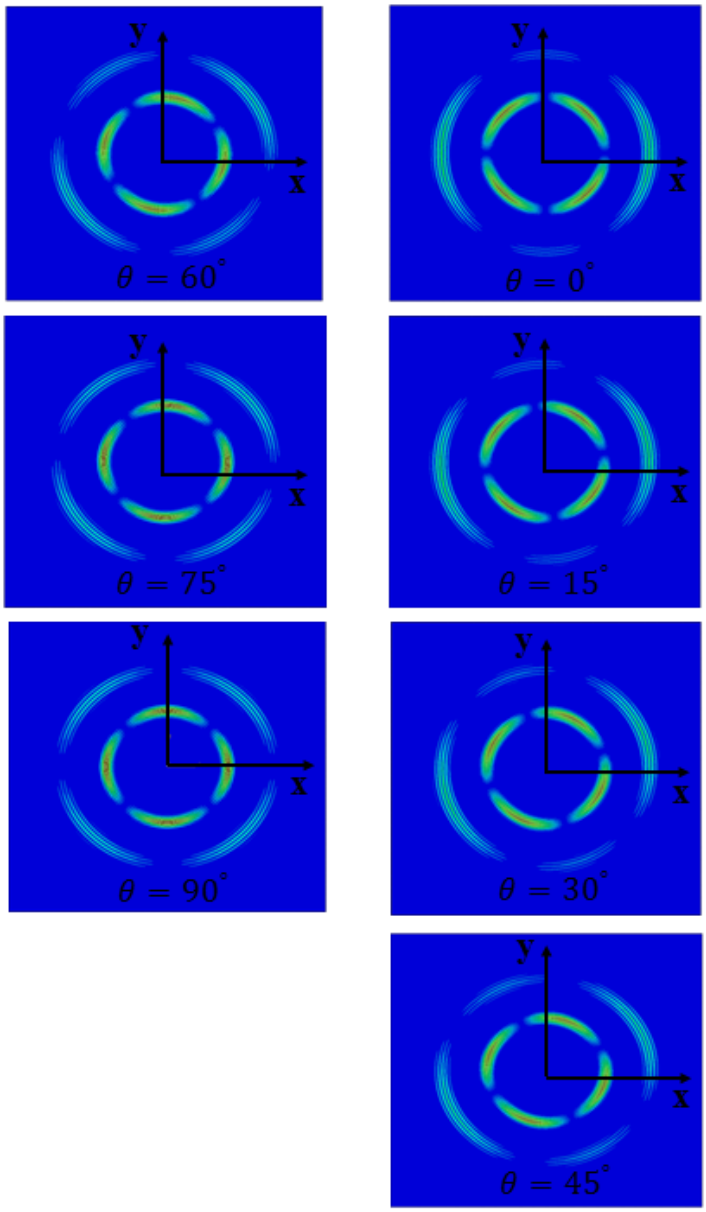

Figure 3.8 Snapshots of the magnitude of the displacement in a plate excited by an OPMT at η = 300 kHz (time = 6.0E-05s). The angle (θ) between $\mathbf{H}_D$ and $\mathbf{H}_S$ is from 0° to 90° with increment of 15°.

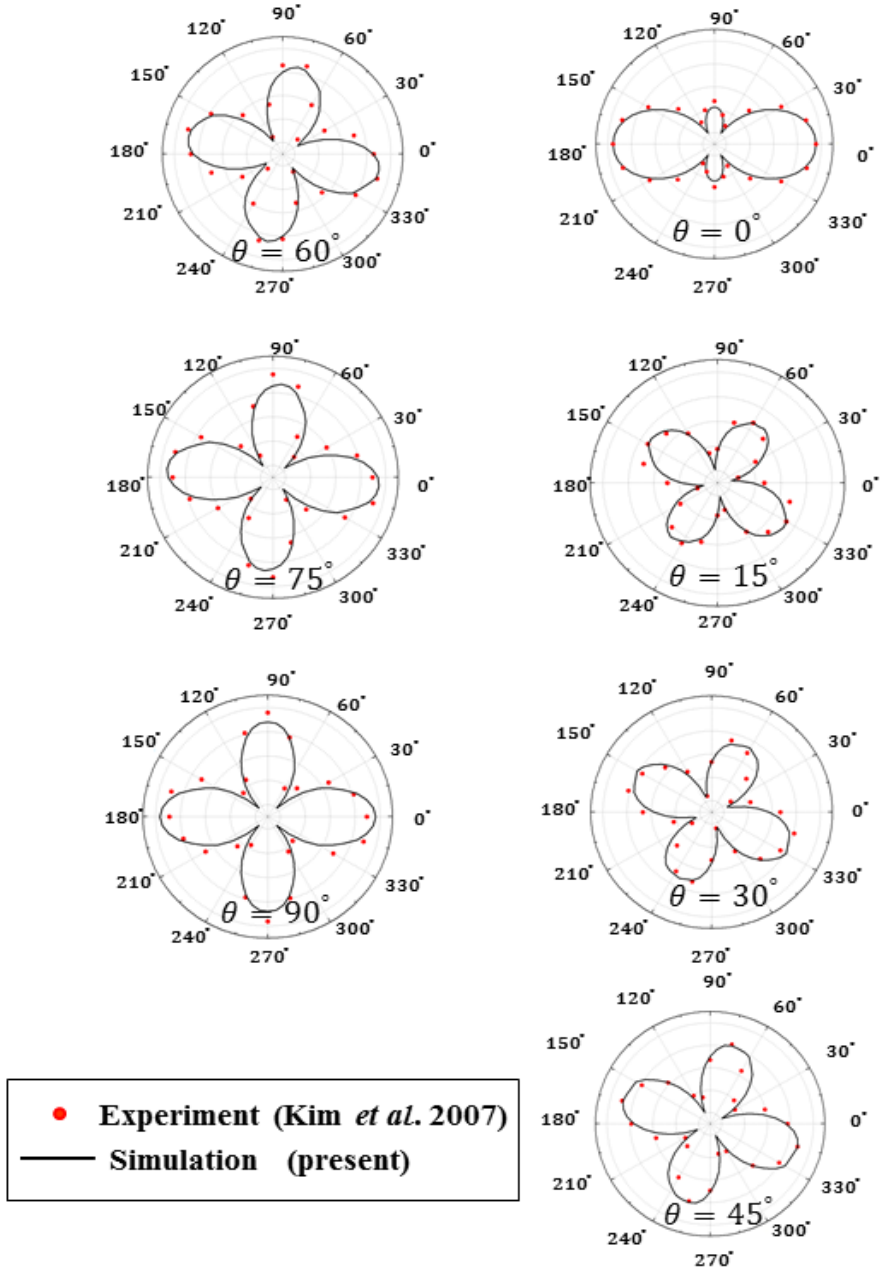

Figure 3.9 Radiation pattern of the S_0 Lamb waves for various angles of θ

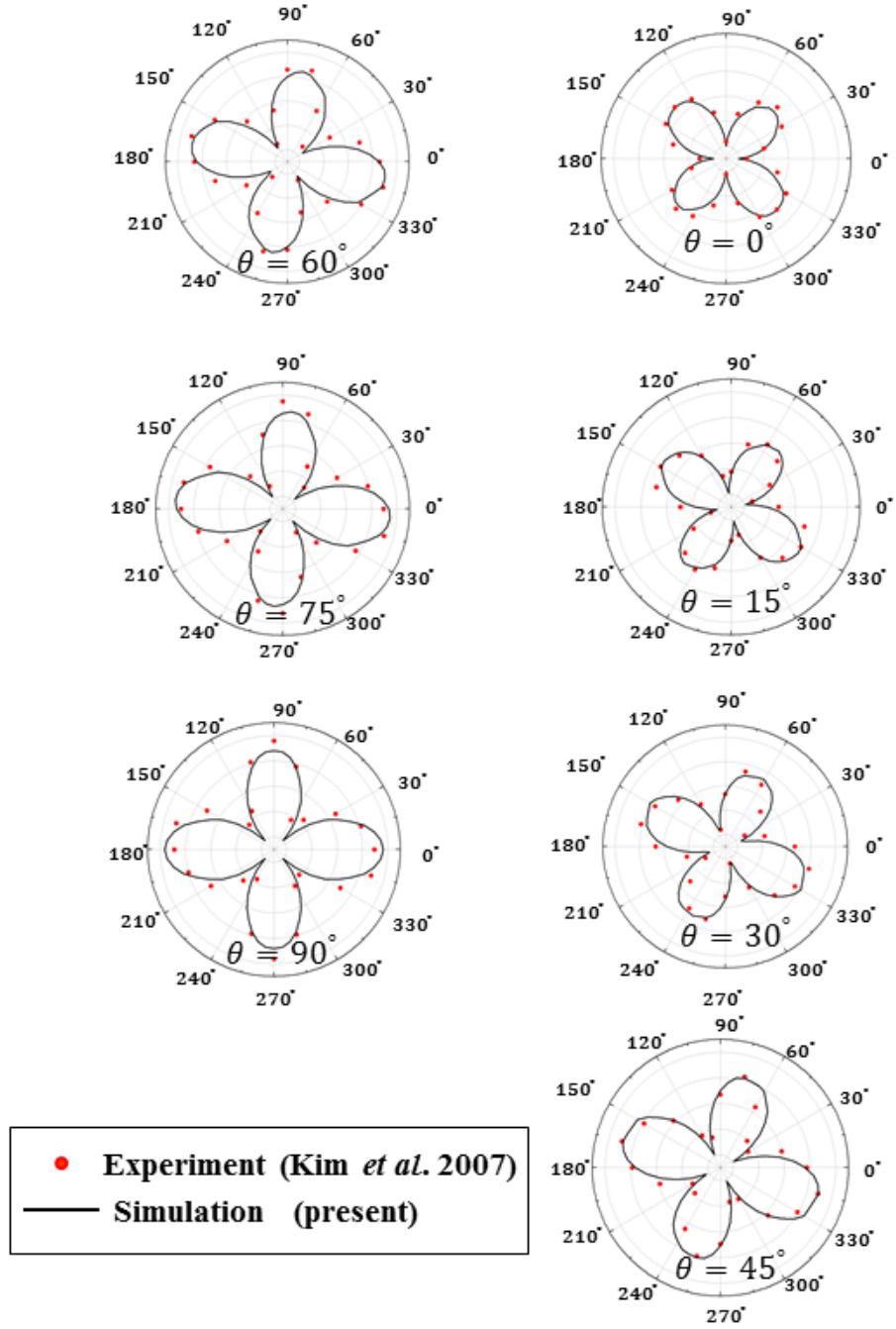

Figure 3.10 Radiation pattern of the SH_0 waves for various angles of θ

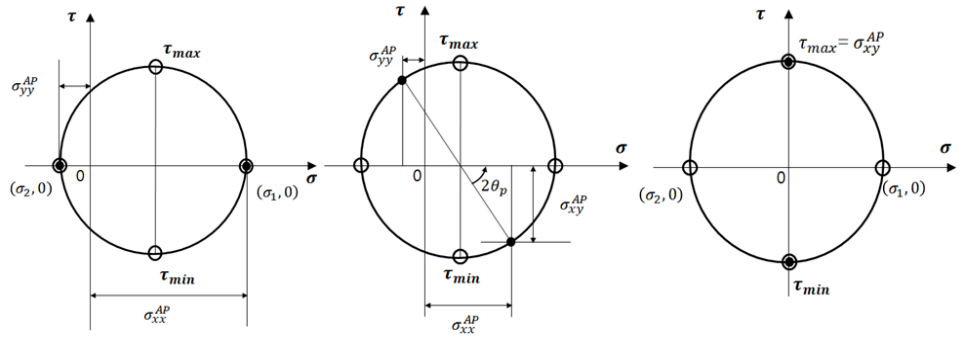

Figure 3.11 The Mohr's circle in a plate excited by an OPMT. The angle (θ) between $\mathbf{H}_D$ and $\mathbf{H}_S$ is (a) 0°, (b) 45°, and (c) 90°.

CHAPTER 4
BEAM-FOCUSED SH WAVE GENERATION BY A CIRCULAR MPT USING A PLANAR SOLENOID ARRAY (PSA)

4.1 Introduction

The accuracy and efficiency of NDE depends on various factors such as the wave power, directivity, mode types, and frequency tuning (Lin and Giurgiutiu (2006), Park *et al.* (2006), Kannan *et al.* (2007), Sundaresan *et al.* (2002), and Kim (2005)). Among these various factors, this chapter focuses on finite element simulation of the wave directivity and frequency tuning characteristics of a magnetostrictive transducer.

Although the conventional single strand meander coil offers good directivity and frequency tuning characteristics, the induced magnetic field is not enough to generate high-power ultrasonic waves. So its directivity needs to be further improved to achieve higher-resolution NDE. Several turns of the figure-of-eight coil in the transducer enable the power of SH_0 wave to increase (Cho *et al.* (2006)). As an alternative means to improve the directivity or frequency tuning characteristics, a meander coil was introduced. It has been adopted in electromagnetic acoustic transducers and magnetostrictive transducers (Murayama (1996), Hiro and Ogi (2003), and Murayama *et al.* (2004)). Lee *et al.* (2007) proposed a newly developed specially-configured meander coil-type configuration to produce high-power wave with

higher frequencies as shown in figure 4.1. In this chapter, the wave generation mechanism of the transducer in figure 4.1 will be explained and a number of finite element simulation related to wave directivity will be carried out and validated by available experiments (Lee *et al.* 2007). The wave radiation patterns obtained from the experiments will be compared with those obtained by using an equivalent source modeling methods employing a concept of distributed line source model.

4.2 Experimental Setup of PSA-OPMT

Experiments of radiation pattern of the Lamb and SH waves in PSA-OPMT were conducted by Lee *et al.* (2009) and these available experiment results were used as reference data for simulation results. Experiment procedures performed by Lee *et al.* (2009) are briefly introduced for better understanding the experimental results. The experimental setup is illustrated in figure 4.2. Circular magnetostrictive patches made of nickel (diameter: 24 mm, thickness: 0.15 mm) were attached on a 3 mm thick aluminum plate. Two PSA-OPMT's were used for the transmitter and receiver. In the receiver, PSA converts the dynamic mechanical strain of the circular patch into voltage. The orientation of PSA in the receiver is along the dotted line connecting from the center of transmitter to the center of receiver. The distance d between the transmitter and the receiver was fixed at 300 mm in this experiment. For all experiments, a Gabor function $f_{Gp}(t)$ defined in

previous chapter was used (Hong *et al.* (2005)). The Gabor pulse signal input of the transmitter is generated by a function generator (HP35670A) and amplified by an amplifier (RITEC RAM-5000). The output voltage of the receiver is measured by a preamplifier (SR560) and sent to an oscilloscope (LeCroyLT-354M). In the experiments, the excitation frequencies between 200 kHz and 500 kHz were used. Because only non-dispersive SH_0 exists under the first cutoff frequency $f_c = 510\,\text{kHz}$; see the dispersion curve of the SH wave in figure 4.3.

4.3 Equivalent Source Modeling of PSA-OPMT

The PSA-OPMT is possible to generate either the Lamb wave or the SH wave because the generated dynamic magnetic field is virtually unidirectional as shown in figure 4.4 (b) (Lee *et al.* 2009). The dynamic magnetic field of nickel patch is concentrated along the straight current wire and its direction is determined by right hand rule. The directions of static magnetic field of PSA-OPMT are same as x-axis.

As explained in introduction, the dynamic field is parallel with (or perpendicular to) the static field, the Lamb wave (or the SH wave) alone will be generated in the plate. Because the dynamic strain field is mainly responsible for wave generation in a plate through mechanical deformation in a patch, we will be mainly focused on the dynamic field as force sources. In the presence of a bias static magnetic flux, the

dynamic magnetic field generates the traction forces within the nickel patch according to equation (3.3). The derivation of the resulting traction force distribution on the aluminum plate is the key in this analysis. Once the forces are determined, they will be used as the driving forces in purely-structural finite element analysis. Note that the dynamic magnetic fields are generated through the coils into which an alternating electric current is flown.

Let us now generate the equivalent distributed force model in case of the PSA-OPMT consisting of four planar solenoids ($N = 4$) shown in figure 4.5 (a). Assume that an input current is sent to the coils in the PSA-OPMT. In the input shown in figure 4.5 (a), the current is flown in the counterclockwise direction in the first (top) planar solenoid and the current in second planar solenoid, in the clockwise direction. The same patterns are repeated in the third and fourth planar solenoids. The resulting dynamic magnetic field generated by these currents is indicated by big arrows in figure 4.5 (a). Note that the field is concentrated around three regions in the magnetostrictive patch indicated by symbols m = 1, 2 and 3. The static bias field is mainly along the x direction and figure 4.5 (b) illustrates the direction of the static and dynamic fields on the circular magnetostrictive patch. Obviously, the direction of the dynamic magnetic field is reversed as the applied input current varies at a certain frequency. When PSA-OPMT's are employed, the distance (D) between each solenoid was so selected as to generate a Gabor pulse of the center frequency η most

efficiently. As argued in the earlier studies (see, e.g. Lee *et al.* 2009), the distance D is selected to be

$$2D \cong \lambda \tag{4.1}$$

where λ is the wavelength to be excited. Therefore, the line source model as employed in (Lee *et al.* 2009) can be adopted here and along the source line, the distributed force formula given by equation (3.12) can be used. For instance, $\theta = 90^{\circ}$ (which corresponds to the case illustrated in the PSA-OPMT configuration in figure 4.5 (a)), we prescribe the distributed loads along the three narrow regions (*m* = 1, 2, 3) in the patch as

$$\begin{aligned} q_x &= \frac{cEd_{11}H_D}{(1+\nu)}\frac{3\zeta}{2}\sin\gamma \\ q_y &= \frac{cEd_{11}H_D}{(1+\nu)}\frac{3\zeta}{2}\cos\gamma \end{aligned} \tag{4.2}$$

Figure 4.6 (a) illustrates the distributed forces applied along the boundary of the narrow rectangular regions (*m* = 1, 2, 3). If $\theta = 0^{\circ}$, the distributed forces become

$$\begin{aligned} q_x &= \frac{cEd_{11}H_D}{(1-\nu^2)}\frac{(2-\nu)}{2}\cos\gamma \\ q_y &= \frac{cEd_{11}H_D}{(1-\nu^2)}\frac{(2\nu-1)}{2}\sin\gamma \end{aligned} \tag{4.3}$$

The resulting distributed forces along the boundary of the rectangular regions are illustrated in figure 4.6 (b). Note that the suggested distributed force model can be valid as long as far field elastic wave field in a plate is of the main interest, which is the case in the present study. The exact traction forces depend on the dynamic magnetic field strength that is not uniform but along the source lines, they are assumed to be uniform. The detailed loading conditions of PSA-OPMT's will be explained later in finite element simulation.

4.4 Finite Element Simulation and Verification

In case of PSA-OPMT's, two cases are considered with the relative angle between the dynamic magnetic field direction and the static magnetic field direction. In the first case, the actuating dynamic magnetic field ($\mathbf{H_D}$) produced by the solenoid is perpendicular to the static field ($\mathbf{H_S}$) as shown in figure 4.7 (a). Table 4.1 lists the details of the PSA-OPMT's used. As a specific example, consider a planar solenoid array consisting of four solenoids (N = 4) shown in figure 4.7. The magnetic field developed in the magnetostrictive patch due to the current flown in the solenoid can be assumed to be concentrated mainly on the three strip regions indicated by the arrow symbols marked with m = 1, 2 and 3 in figure 4.7. The strip width w_c is 1 mm, which is determined by magnetic analysis (e.g., by using COMSOL). Because magnetic fields in other regions of the patch are much smaller than those in the strip regions, the former fields can be ignored for

subsequent analysis. The equivalent distributed forces on the strip regions are calculated by equations (4.2) and (4.3) and they are schematically illustrated. Even if magnetic field strength within each strip is assumed to be uniform, the directions of the equivalent shearing forces change from one strip region to another (i.e., as m is varied). Therefore, the total response at a measurement point $P(x, y)$ is the sum of the alternating shearing forces at the location of an actuating magnetostrictive transducer. The actuation frequencies considered for the cases in figures 4.7 (a) and (b) are $\eta = 250$ kHz and 430 kHz, respectively. (These frequencies were selected in experiments conducted in (Lee *et al.* 2009).)

4.4.1 Wave Radiation Analysis in a Plate Excited by PSA-OPMT

Let us consider further wave simulation in the aluminum plate (thickness : 3 mm) considered in section 3.2 but this time, PSA-OPMT's are used as a transmitter and a receiver. The dimensions of the circular nickel patches used in PSA-OPMT's are 24 mm in diameter and 0.15 mm in thickness. To check the validity of simulation results obtained by using the proposed equivalent distributed force model, we use the same condition as used in the earlier experiment (Lee *et al.* 2009). The experimental setup is the same as the one shown in figure 4.2. The results in figure 4.8 are obtained with the PSA-OPMT configuration depicted in figure 4.7 (a) while those in figure 4.9, with that in figure 4.7 (b). The radiation patterns plotted as a function of α

show that the present equivalent distributed force model replacing PSA-OPMT's correctly captures the main lobes with slight deviations in side lobes. The inaccuracy in the prediction of the side lobes is due to several assumptions made for the present model. Idealized uniform magnetic field was assumed for the strip regions with the fixed width of 1mm for each strip region in the magnetic patch and the magnetic fields in other regions of the patch were not considered. Nevertheless, the normalized amplitudes in stress at the main lobe are accurately predicted by the proposed force model. From the numerical results in figures 4.8 and 4.9, one can conclude that PSA-OPMT's are more effective in focusing wave energy along a specific direction than OPMT's. Further, the wave energy is flown along the direction of the applied magnetic field. Although not shown here, it is also numerically confirmed that the wave directivity is improved as the coil interval *D* becomes smaller.

4.4.2 Interaction of SH_0 waves with a oblique crack

To investigate the interaction between oblique incident SH waves and a through-thickness crack, oblique crack angles $\beta = 0^{\circ}$, 30°, 60°, and 90° were considered. The size of the crack, 20mm×1mm, was introduced with a central position (x=0 mm, y=200 mm) in a coordinate system with its origin at the center of the plate as shown in figure 4.10. The crack was simulated by removing the equivalent element. The isotropic plate was modeled using CPS4R (4-node bilinear plane stress

quadrilateral with reduced integration), which are computationally efficient and accurate.

In crack analysis, only the SH_0 wave of PSA-OPMT is investigated. Figure 4.11 shows the scattering phenomena such as transmission, reflection and mode conversion according to the change in crack angle β in case of SH_0 with 250 kHz. The reflected stress $\sigma_{r\theta}$ was measured at r = 100 mm on the basis of the local cylindrical coordinate created at the crack center as measuring angle α was varied from -90° to 0° by 30° increment. Figure 4.12 shows that the relative simulated amplitude of the scattered signals SH_0 agrees quite closely with the measured ones. The oblique angle of crack has an important effect on amplitude of scattered wave signals collected by sensors. As expected, the reflected amplitude of SH_0 at $\alpha = -90^{\circ}$ is the largest in the case of $\beta = 0^{\circ}$, and the reflected amplitude decreased as the measuring angle α is increased. In case of $\beta = 30^{\circ}$ and 60°, the reflected modes from crack at $\alpha = 0^{\circ}$ is larger than those measured by other angle. The smallest reflected amplitude was occurred in case of the direction of both SH_0 wave and crack is parallel.

4.5 Summary

The equivalence source modeling employing a distributed line source model for PSA-OPMT was developed. The radiation pattern or the directivity obtained from the experiments agreed favorably with a finite

element simulation. The use of planar solenoid arrays in the magnetostrictive transducer effectively oriented the generated SH wave along the direction of the dynamic magnetic field of the transmitting transducer. As the solenoid interval in PSA decreased and the actuating frequency increased, the directivity of the generated wave was improved accordingly. When the actuation frequency was selected to be below the first cutoff frequency of the SH wave mode, only the non-dispersive SH_0 wave was simulated by the suggested equivalence source modeling methods.

Table 4.1 Data used for the present wave simulation with PSA-OPMT's

N	D (mm)	$\lambda(=2D)$ (mm)
4	6.2	12.4
6	4.2	8.4

(N: the number of planar solenoids, D: distance between coil lines)

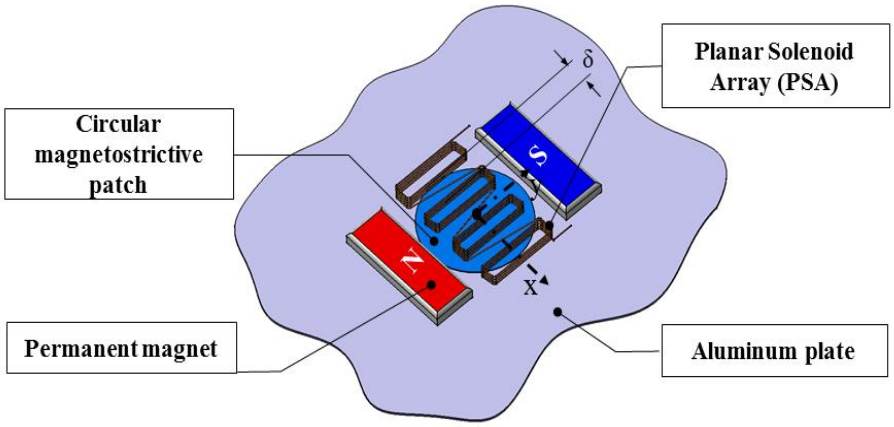

(b)

Figure 4.1 Magnetostrictive patch transducers using a planar solenoid array coil (Lee *et al.* (2009)). (In actual configuration $\delta \cong 0$). Note that the transducers are called a PSA-OPMT (PSA: Planar Solenoid Array).

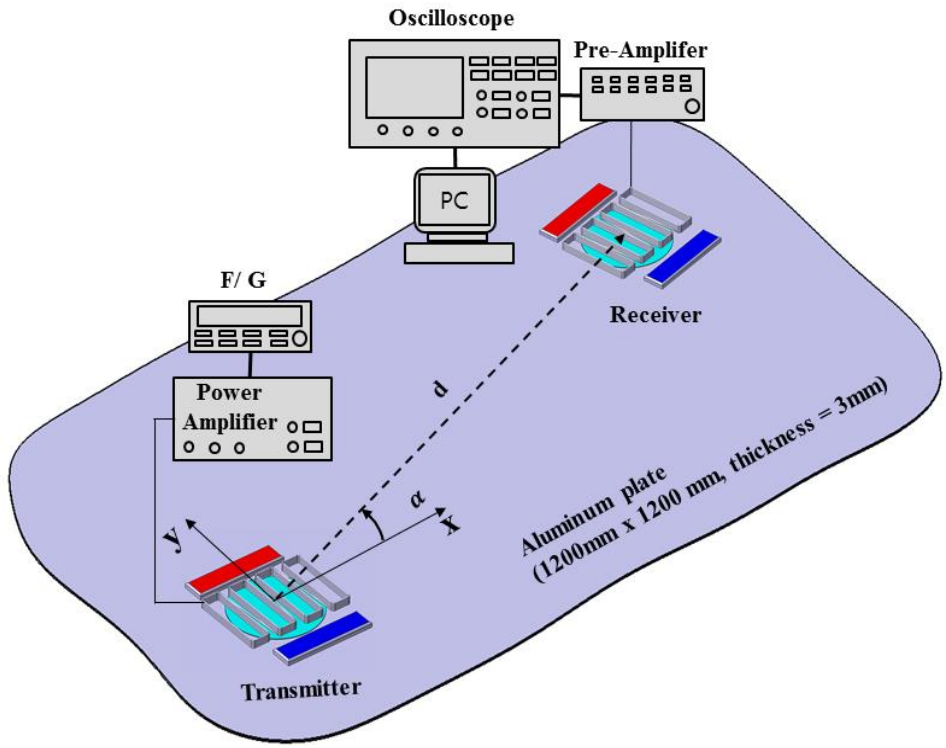

Figure 4.2 Experimental setup in a plate by using PSA-OPMT's.

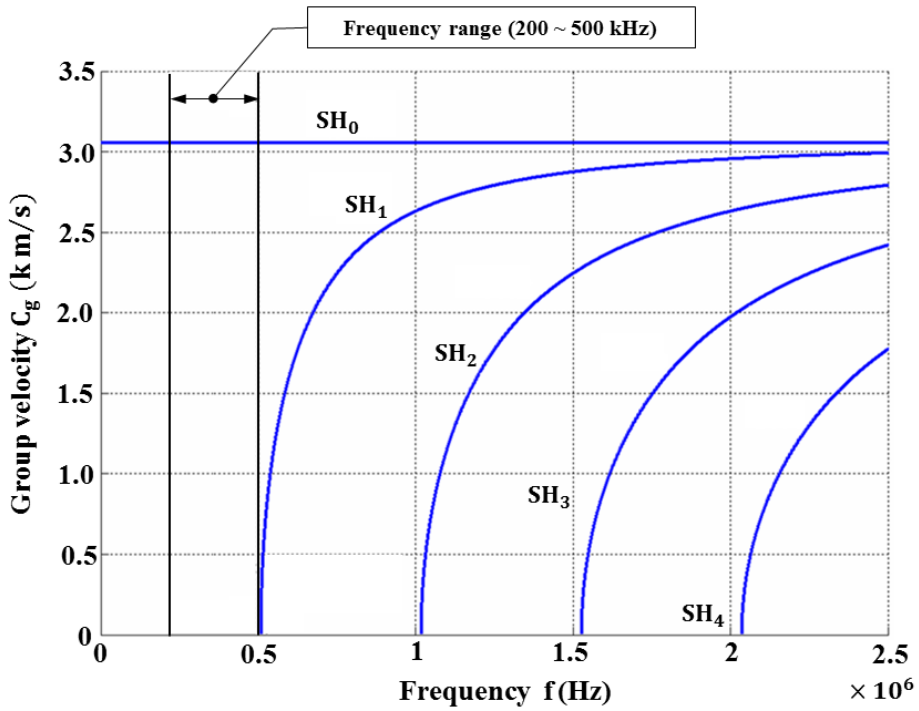

Figure 4.3 The dispersion curve of the SH wave mode in a 3mm thick aluminum plate.

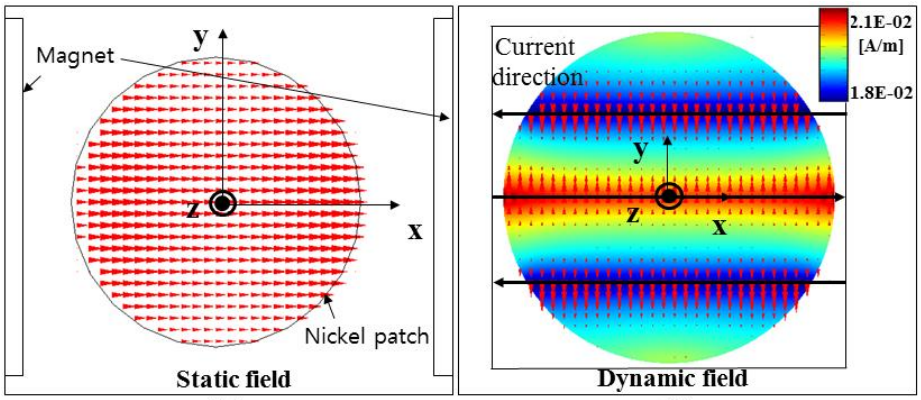

Figure 4.4 (a) The static and (b) dynamic magnetic field distributions induced by a planar solenoid array (PSA) coil.

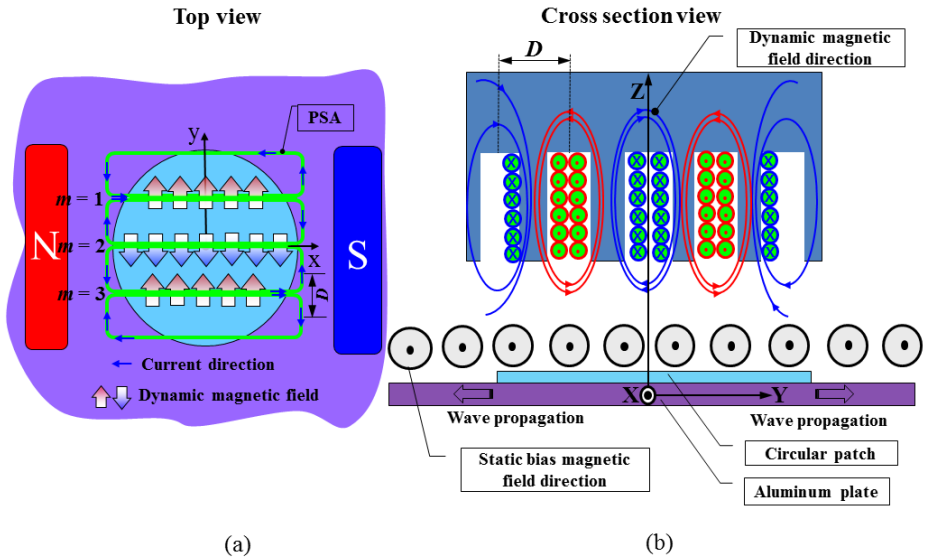

Figure 4.5 (a) The direction (marked by big arrows) of dynamic magnetic field by planar solenoid coils in the PSA-OPMT transducer and (b) the cross sectional view of the PSA-OPMT.

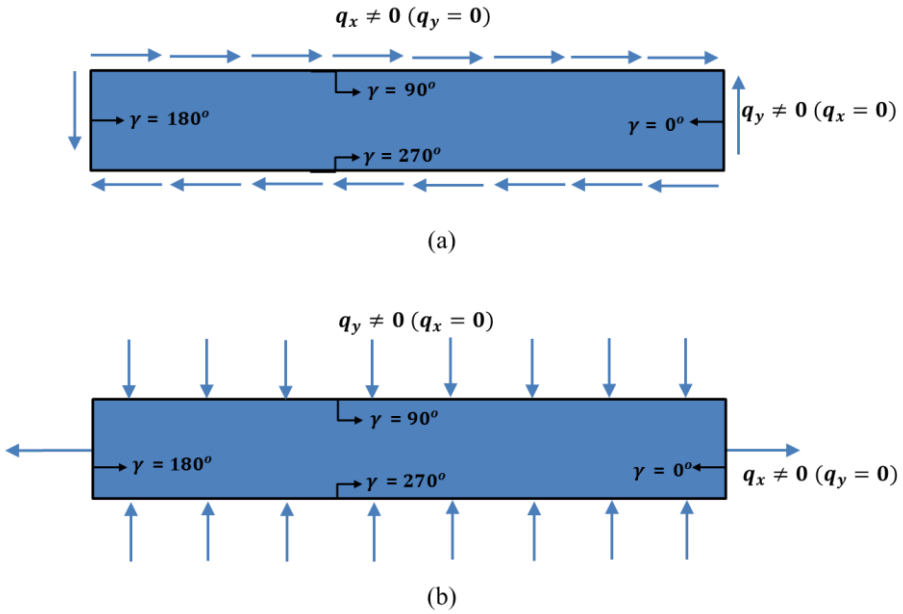

Figure 4.6 Illustration of the distributed forces in strip regions of the circular magnetostrictive patch in a PSA-OPMT for (a) $\theta = 90^{\circ}$ and (b) $\theta = 0^{\circ}$.

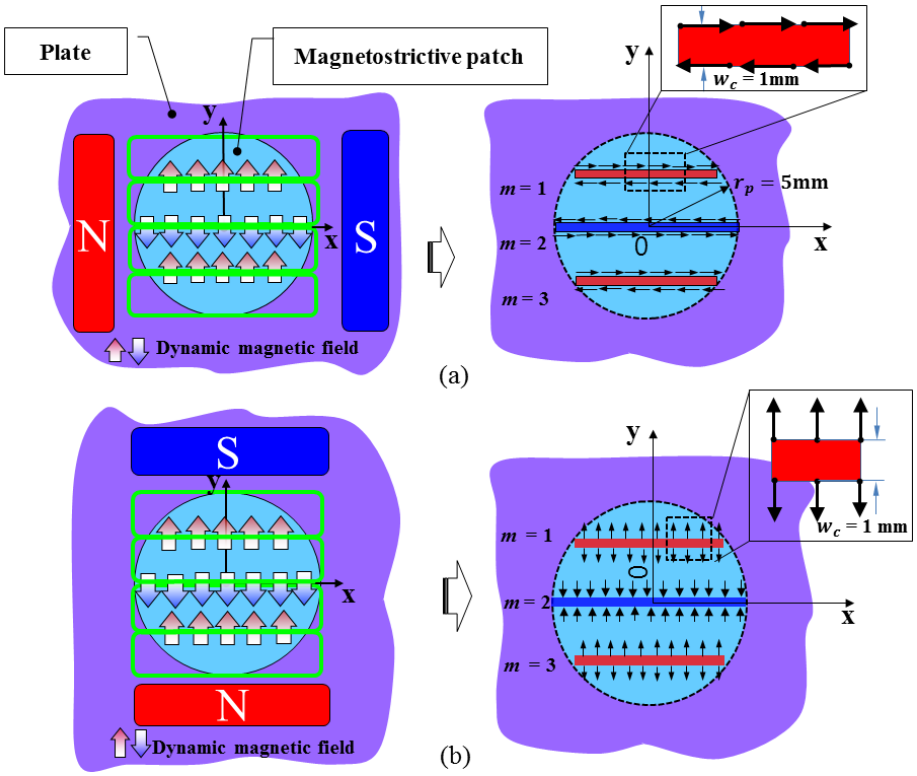

Figure 4.7 The equivalent distributed force model used for PSA-OPMT's for (a) the SH-wave generation and (b) the Lamb wave generation.

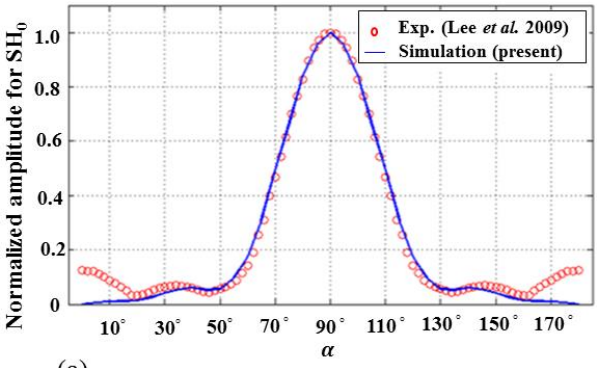

(a)

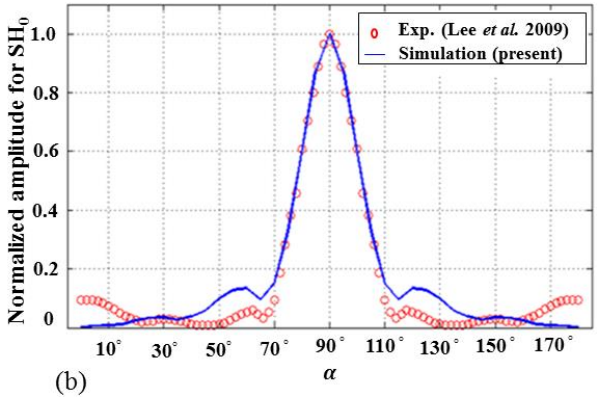

(b)

Figure 4.8 The stress radiation pattern in a plate excited by PSA-OPMT's for SH wave generation at time = 9.0E-5 [s]. (a) η = 250 kHz and (b) η = 360 kHz.

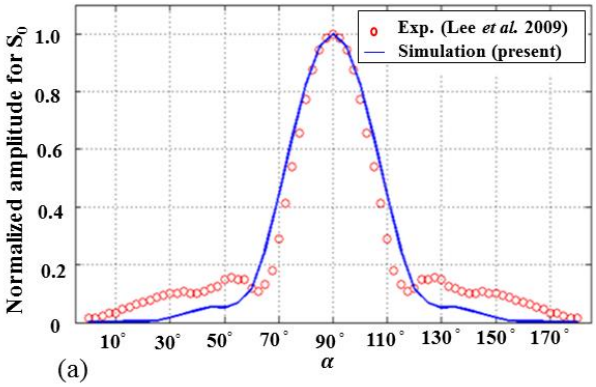

(a)

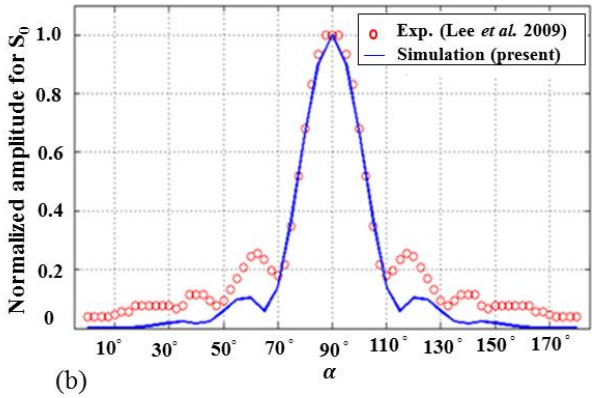

(b)

Figure 4.9 The stress radiation patterns in a plate excited by PSA-OPMT's for Lamb wave generation at time = 5.0E-05 [s]. (a) η = 430 kHz and (b) η = 635 kHz.

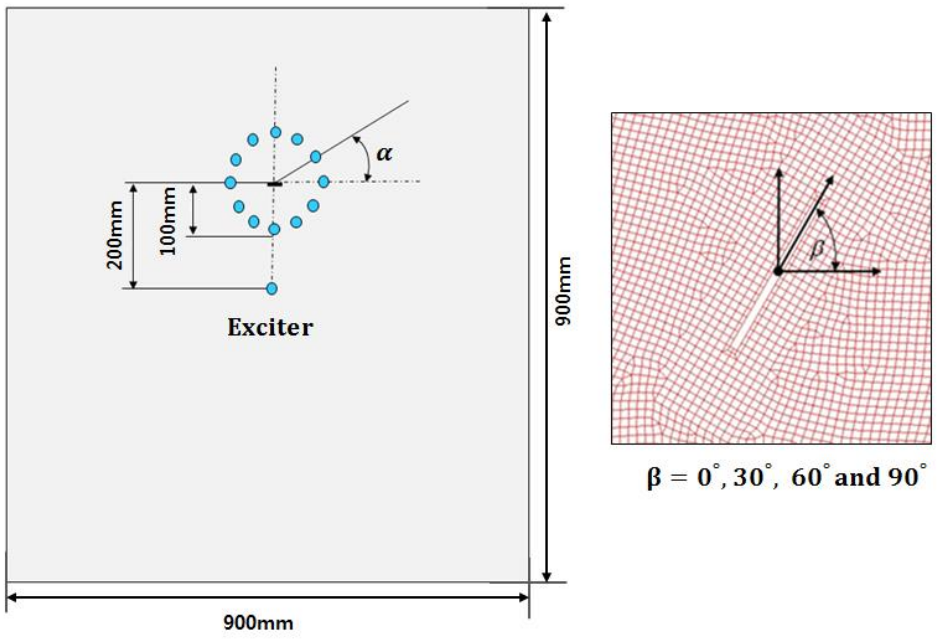

Figure 4.10 Oblique crack (20mm × 1mm) modeling in case of PSA-OPMT.

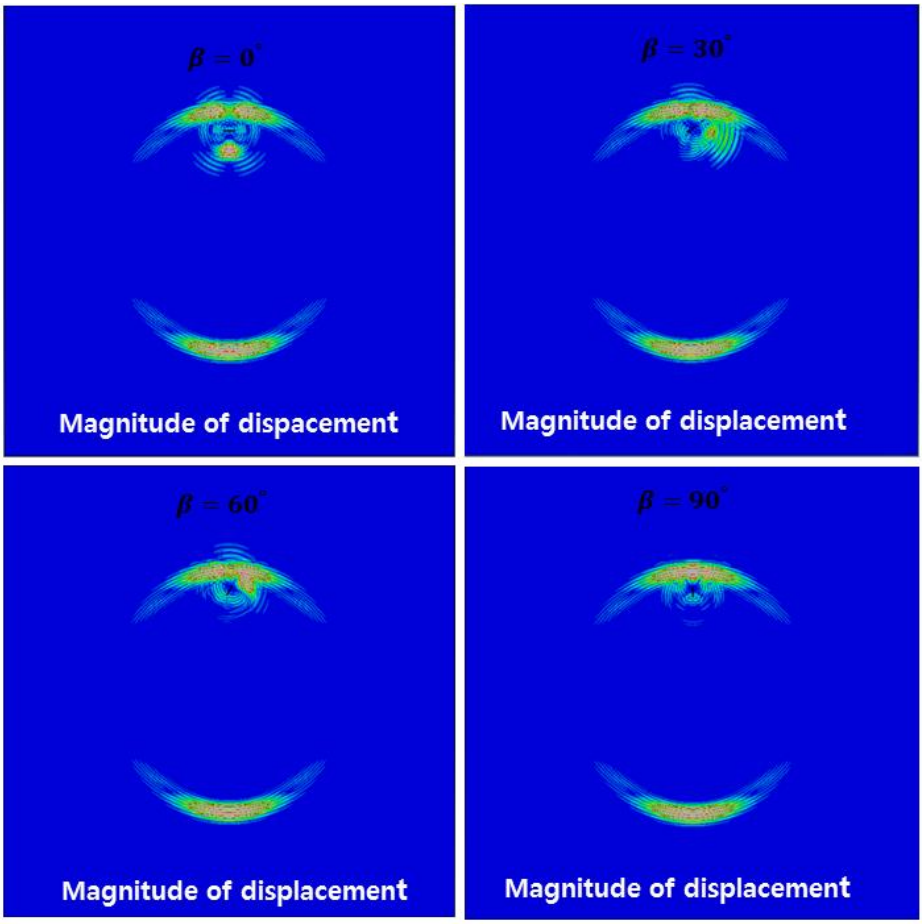

Figure 4.11 Snapshots of the displacement magnitude of reflected SH waves in a plate excited by a PSA-OPMT at η = 250 kHz (time = 9.0×10^{-5}s).

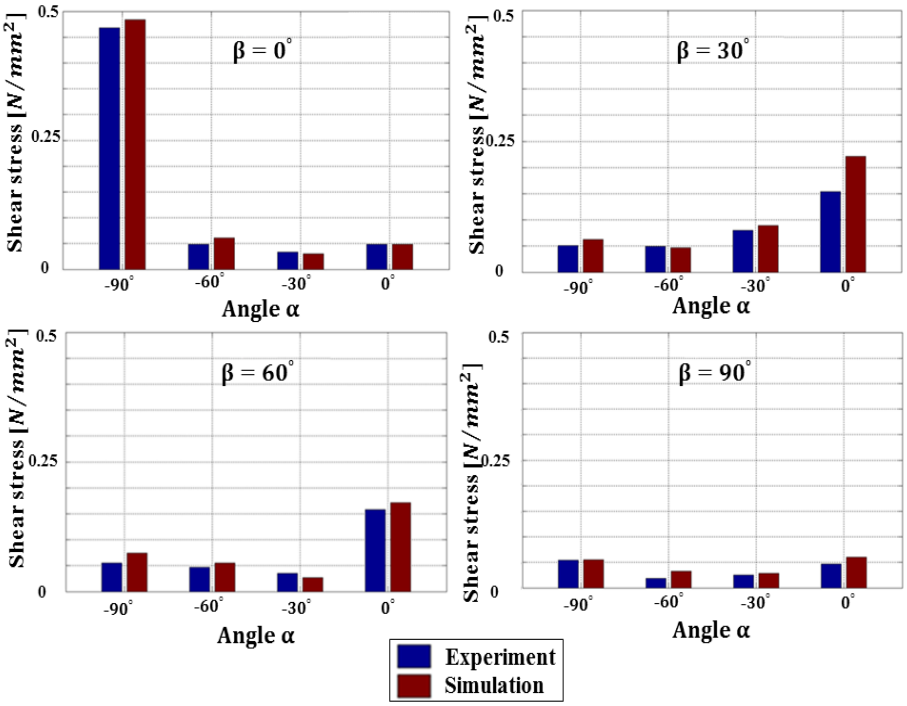

Figure 4.12 Stress amplitude of reflected $\sigma_{r\theta}$ waves at 250kHz around the crack after the interaction with 20mm × 1mm crack.

CHAPTER 5

TORSIONAL AND SHEAR-HORIZONTAL WAVE BASED PIPE DAMAGE INSPECTION BY MAGNETOSTRICTIVE TRANSDUCER

5.1 Introduction

Magnetostrictive patch transducers have been used effectively for not only plate but also pipe inspection. Torsional wave whose fundamental mode is non-dispersive has been adopted to inspect defects in cylindrical structures. In this study two types of magnetostrictive patch transducer will be investigated by using finite element simulation employing the equivalent source modeling of transducer ; one is the segmented-patch-array magnetostrictive transducer for detecting the axial and circumferential crack. The other is specially-configured magnetostrictive patch transducer developed for detecting axial crack by using the helically propagating SH waves.

Firstly, a conventional single transducer consisting of a solenoid coil and magnetostrictive patches can detect axial defect, but can't detect circumferential defects (Kwun (2002), Cho *et al.* (2005), Park *et al.* (2006) and Kannan *et al.* (2007)). Recently, Kim *et al.* (2011) developed a new type of magnetostrictive patch transducer that can detect the axial and circumferential defects simultaneously. The main idea of the proposed transducer is to use a segmented patch array

transducer to send SH waves over the cylindrical surface of a target pipe as shown in figure 5.1 (a). A number of patch pieces are bonded over the pipe in circumferential direction and each patch piece generates and measures SH waves.

Secondly, although the torsional wave is useful for detection not only circumferential cracks but also axial cracks in pipes, the induced electric field of receiver can't give enough information to identify the axial crack when the reflection coefficient of the axially propagating torsional wave to axial crack is negligibly small. Demma *et al.* (2003) demonstrated that reflection coefficient is roughly proportional to the cross-sectional area of the defect. Kim *et al.* (2013) proposed structural health monitoring methods for an axial crack with helically propagating shear-horizontal waves that are generated by a specially-configured magnetostrictive patch transducer as shown in figure 5.1 (b).

The objective of this study is to develop an equivalent source modeling methods for segmented patch array transducer and specially-configured magnetostrictive transducer. Several available experiments to find the circumferential and axial cracks on a pipe were used to validate the newly suggested equivalent source modeling methods.

5.2 Experimental setup

Experiments for detecting circumferential and axial cracks were

conducted by Kim *et al.* (2011 and 2012) and these experiment results were used as reference data for simulation results. Experiment procedures performed by Kim *et al.* (2011) are briefly introduced for better understanding the experimental results.

Firstly, figure 5.1 (a) shows the configuration of the developed segmented-patch-array mangetostrictive transducer. It consists of segmented magnetostrictive patch pieces bonded onto a pipe, meander coils, and permanent magnets. The permanent magnet (neodymium magnet, 3x3x25mm) is placed between patches and supplies the static magnetic field to the patch in the circumferential direction. The permanent magnets are arranged in order to generate the uniform static magnetic field in all patches. On the other hand, the dynamic magnetic field is applied to the patch segments in the axial direction by the current flowing into the meander coil. When the static and dynamic magnetic fields are superposed perpendicularly, the patch experiences shear deformation resulting from magnetostriction (Thompson (1978)). Then, the shear-horizontal wave propagated along pipe. Because the meander coil acts as a wavelength filter, high-frequency SH_0 wave can be effectively generated by controlling the line interval between adjacent meander lines same as half the wavelength at a given excitation frequency (Cho *et al.* (2010)). An iron-cobalt alloy (Hiperco 50HS, Carpenter Technology Corp., Wyomisssing, PA) was used to make the magnetostrictive patches. The test pipe is a seamless stainless steel pipe of 76.4 mm in outer diameter and 2.1 mm in thickness.

Secondly, the specific configuration of the developed transducer is shown in figure 5.1 (b). It consists of two rectangular mangetostrictive patches that are bonded onto a pipe through epoxy resin. It employed a permanent magnet (Neodymium magnet, 3×3×25 mm) and a figure-of-eight coil. Static magnetic field is applied to the two patches in the circumferential direction by the permanent magnet placed between the two patches and dynamic magnetic field is in the axial direction by the current flowing perpendicular to each other, the patch experiences shear deformation by the mangetostriction effect, the coupling effect between magnetic field change and mechanical deformation (Thompson (1978)). This is the generation mechanism of SH wave by the transducer in the waveguide while the reversed mechanism applies to SH wave sensing. A brass pipe of 28.85mm in outer diameter, 1.05mm in thickness and 1500mm in length was used as a test pipe and two transducers were installed. The distance between the two transducers was 300mm. An iron-cobalt alloy was used to make the magnetostrictive patches of 20mm in length (l_p), 3mm in width (w_p) and 0.15mm thickness. The grating distance (d_p), the distance between the centers of two patches, was 6mm. The input signal to the transmitting transducers was a Gabor pulse at 375 kHz. If the excitation frequency of the SH wave is below the first cut-off frequency, only the non-dispersive first-branch SH_0 wave is generated. Experiments are conducted in the pitch-catch mode throughout the present study.

5.3 Equivalent Source Modeling of SH wave

Let us now study how equivalent distributed force models can be developed for MPT's when they are applied to pipes. In case of the segmented-patch array transducer shown in figure 5.1 (a), slender permanent magnets are placed over segmented magnetostrictive patches at an interval of 60° along the circumferential direction. One may assume that static magnetic field is distributed uniformly in the circumferential direction (θ). In cylindrical coordinate, the equation (3.4) can be written as

$$\begin{Bmatrix} \varepsilon_{\theta\theta}^{NP} \\ \varepsilon_{zz}^{NP} \\ \varepsilon_{\theta z}^{NP} \end{Bmatrix} = \begin{bmatrix} d_{11} & 0 & 0 \\ d_{12} & 0 & 0 \\ 0 & d_{35} & 0 \end{bmatrix} \begin{Bmatrix} H_\theta \\ H_z \\ H_r \end{Bmatrix} \tag{5.1}$$

With similar assumption of continuity of strain components between pipe and nickel patch, stress components of stainless steel pipe are written as

$$\begin{aligned} \sigma_{\theta\theta}^{SP} &= \frac{E d_{11}}{(1-\nu^2)} \left(\frac{2-\nu}{2} \right) H_\theta \\ \sigma_{zz}^{SP} &= \frac{E d_{11}}{(1-\nu^2)} \left(\frac{2\nu-1}{2} \right) H_\theta \\ \sigma_{\theta z}^{SP} &= \frac{E}{2(1+\nu)} d_{35} H_z \end{aligned} \tag{5.2}$$

The superscript SP stands for "Stainless steel Pipe". In pipe the

dominant component of dynamic magnetic field generated by meander coil is H_z and other components are negligible ($H_r = H_\theta \cong 0$). Therefore, non-zero stress component in equations (5.2) is $\sigma_{\theta z}^{SP}$. With introduction of definition ζ, piezomagnetic coefficient d_{35} in equation (5.2) can be expressed as $3\zeta d_{11}$. For instance, one can use equivalent distributed forces for the axially-narrow rectangular regions by using $\boldsymbol{q} = c\boldsymbol{n} \cdot \boldsymbol{\sigma}^{SP}$

$$q_\theta = \frac{cEd_{11}H_z}{(1+\nu)}\frac{3\zeta}{2}, q_z = 0 \text{ (along the edge with } \boldsymbol{n} = \boldsymbol{e_z}) \quad (5.3)$$

and

$$q_z = \frac{cEd_{11}H_z}{(1+\nu)}\frac{3\zeta}{2}, q_\theta = 0 \text{ (along the edge with } \boldsymbol{n} = \boldsymbol{e_\theta}) \quad (5.4)$$

Because adjacent lines of the meander coil have opposite current directions, the directions of the applied equivalent dynamic forces change alternatively with the period of the meander coil distance.

5.4 Finite Element Simulation and Verification

5.4.1 SH_0 waves generated by segmented patch transducer in a pipe

We aim to obtain the numerical results by using the present equivalent force model for the experiments (Kim *et al.* (2011)) performed in a pipe with segmented patch transducers. The experimental setup is illustrated in figure 5.2 (a) and 5.3. The symbols T_i and R_j refer to the *i*th

transmitting and *j*th receiving transducer segments, respectively. Figure 5.4 shows the propagation of transient SH_0 waves ($\sigma_{\theta z}$ stress distribution). In figure 5.5, the simulation results are compared with the experimental results for the angular profiles. They are calculated at the axial distances of $x_{lm} = 300$, 900, 1500, and 2500 mm for the excitation frequency of 500 kHz. (For the profile analysis, the pipe without a crack was used). The figure shows that the simulation results agree well with the experimental results (Kim *et al.* (2011)). To plot the angular profile from simulation, the $\sigma_{\theta z}$ component is monitored at the axial location of x_{lm} with a circumferential increment of 5°. For the cracked pipe depicted in figure 5.3 (b), two circumferential through-wall cracks, 12 mm long and 3 mm wide, are made on the pipe at circumferential angles of 120° and 240° relative to the transmitter T_1. Figure 5.6 shows the simulated signals for the $T_3 - R_3$, $T_1 - R_4$, and $T_5 - R_5$ pairs in the test pipe. Here, the pairs $T_l - R_m$ (l, m = 1, 2,…, 6) means that receiving transducer R_m senses the wave generated by the transmitting transducer T_l. The pulses at 0.023μs are the reflected waves from crack 1, and the pulses at 0.036 μs are the reflected waves from crack 2. In case of $T_3 - R_3$ and $T_5 - R_5$ pairs reflected wave appear mainly from crack 1 and crack 2, respectively. In case of $T_1 - R_4$ pairs, two reflected wave from crack 1 and crack 2 appear, but the amplitudes of waves are smaller than those recorded in the earlier cases. The angular distributions of the peak-to-peak values of the reflected signals for crack 1 and crack 2 are plotted in figures 5.7 (a) and (b). In the plots, the distances from the origin denote the

magnitudes of the reflected wave from cracks 1 and 2. Because receivers R_j are located at every 60°, the angular distributions are also marked at every 60°. The comparison shows that the simulation results obtained by the proposed force model and those by the experimental results (Kim *et al.* (2011)) agree favorably. Although the angular profiles in figures 5.7 (a) and (b) are not exactly the same, the predicted results by the proposed model correctly detect the crack locations.

5.4.2 Helically propagating waves generated by specially-configured magnetostrictive patch transducer in a pipe

In order to use the transducer in figure 5.1 (b), it is very informative to analyze its frequency characteristics which shall depend on patch sizes and the radiation pattern of the transducer.

To begin with, let us investigate the frequency characteristics. To send the input pulse most efficiently (and possibly without any pulse form distortion), one should analyze the frequency characteristic of the transducer such as dependence on the grating distance d_p and width of the patch w_p. Because the grating distance and the width role as filter parameters, we set $w_p = d_p/2$ and varied d_p from 6mm, 12mm to 18m. The results are given in figure 5.8 (a). For all the three tested cases, the excitation frequency was varied from 100 kHz to 500 kHz increments of 25 kHz and the maximum peak-to-peak values of measured signals from pitch-catch type experiments were extracted and

normalized. As expected, the maximum-response frequency $w_p = d_p/2$ is the same as $\lambda/2$ (half the wavelength), the resulting constructive interference makes the signal magnitude the largest. Table 5.1 lists the values of the predicted and experimentally-measured ($f^{Exp} = c_s/d_p, c_s =$ the bulk shear wave velocity, 2182.5 m/s) maximum-response frequencies for three values of the grating distance. The predicted frequencies by finite element simulation employing equivalence source model agree well with the experimentally-estimated frequencies.

Let us know explain the repeated appearances of the pulse of the same form in the measured signal. To this end, we will investigate how the generated SH wave by the transmitter shall radiate. As an underlying experiment to reveal the radiation pattern, pitch-catch experiments were conducted in brass plate having the same thickness as the test brass pipe (see figure 5.9). If the radius of a pipe is much larger than its thickness and wavelength of interest, the pattern of wave radiation can be well described in a plate of the same thickness (Velichko and Wilcox (2009)), For the radiation pattern analysis, the magnetostrictive transducers of 20mm in length , 3mm width and 6mm in grating distance were used. The Gabor pulse of 375 kHz (this frequency will be mainly used in actual detection experiments) was used as an input signal. The transmitter was fixed at the center of the plate while receiver was moved from 0° to 90° in increments of 5° relative to the transmitter. The distance between the transmitter and the receiver

was maintained to be 300mm because the distance between the transmitter and the receiver is a tested pipe is 300mm. To make the same measuring condition as that in a pipe, the longer sides of the patches were aligned with the z axis. Figure 5.10 (a) and (b) show the experimental and finite element simulation results of radiation pattern of the developed transducer obtained at 375 kHz, respectively. The magnitudes of measured waves at radiation angles (α) less than 60° are nearly zero and rises rather steeply from 60° to 90°(Kim *et al.* (2012)). We remark that the waves propagating along the direction $\alpha = 0^{\circ}$ (or $\alpha = 90^{\circ}$) in a plate correspond to the longitudinally propagating SH (or circumferentially propagating waves) in a pipe.

Now, we consider the generation of the SH_0 wave in a pipe by an MPT as depicted in figure 5.2 (b). This problem was experimentally studied in (Kim *et al.* (2012)). The distance between the MPT transmitter and the MPT receiver is 300mm. The MPT's used for this case are the ones shown in figure 5.2 (b). Two magnetostrictive patches of w_p = 3 mm, d_p= 6 mm, l_p= 20 mm and thickness = 0.15 mm are used. Because the measured signals in undamaged pipes will be used as reference signals in structural health monitoring (Kim *et al.* (2012)), we should also conduct pitch-catch experiments in a healthy pipe. Figure 5.11 shows the helically propagating SH_0 waves ($\sigma_{\theta z}$ stress distribution) of both healthy and damaged pipes. The Gabor pulse center at 375 kHz is used as an excitation pulse to obtain the results. As shown in figure 5.11 (a), two rays of the SH pulses emanating from the transducer at a

helix angle of $\pm\alpha_n$ $(n = 1,2,\cdots)$ arrive at the receiver simultaneously at time t_n, $(t_n = L_n/C_{SH_0}$, $L_n = \sqrt{L_1^2 + [2(n-1)\pi\bar{r}]^2}$, $\cos\alpha_n = L_1/L_n$; C_{SH_0}: shear wave speed of SH_0 mode, L_1: axial distance between the transmitter and the receiver, $\bar{r}$: mean radius of a test pipe) . The rays of SH waves emanating at other helix angles ($\alpha_{n'}$ with $n' \neq n$) can be also sensed by the same receiver. The increasing and then decreasing patterns of the peaks in figure 5.12 are known to be due to the radiation pattern of the transducer and damping (Kim *et al.* (2012)). There is a time delay in the peak arrival time between the simulation and experimental results in figure 5.12. The discrepancy is due to difference in measurement methods between the two results. In the experiment, the output voltage of the receiver was measured over the finite patch when the amplitude of the Gabor pulse reached its maximum, while in the simulation, the signal was measured immediately after excitation at point. Nevertheless, the time interval between two consecutive peaks by the simulation is virtually identical to the time interval by the experiment.

Furthermore, let us consider the damaged pipe shown in figure 5.2 (b). In the damaged pipe, an artificial axial notch of $l_c = 10$ mm in axial extent and $w_c = 3$ mm in circumferential extent is used. The distance from the transmitter and the receiver is 150 mm. The simulation results are compared with the experimental results (Kim *et al.* (2012)) in figure 5.13. In both plots of figure 5.13, signals measured in the cracked pipe are to be compared against those in the uncracked pipe for health

monitoring. The Hilbert-transformation of the measured signals is used to plot the magnitudes in figure 5.13. The overall signals patterns by the present simulation and the experimental result match favorably. The figure shows that the present simulation results based on the equivalent distributed force model of the actuating MPT can be used for accurately estimating the structural health of inspected pipes.

Table 5.1 The maximum-response frequencies for varying grating distances (d_p)

d_p [mm]	f^{Pred} [kHz]	f^{Exp} [kHz]
6	363	375
12	181	200
18	121	125

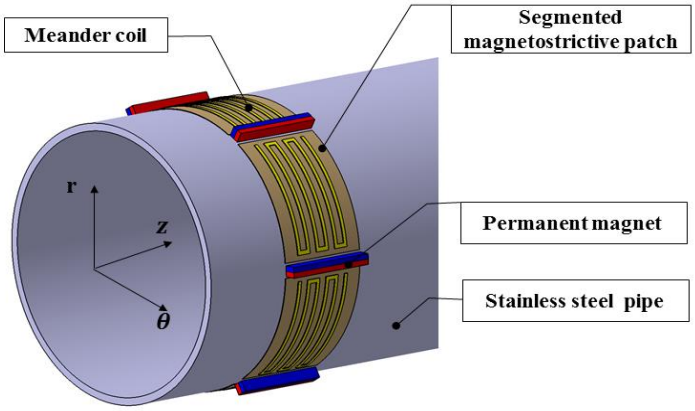

(a)

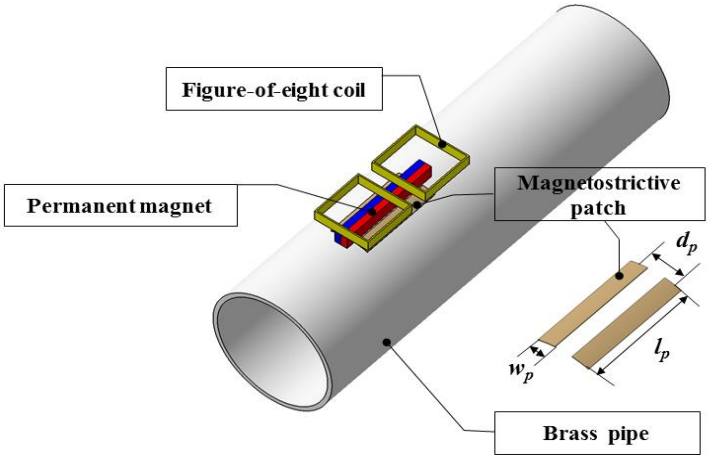

(b)

Figure 5.1 (a) A segmented-patch-array magnetostrictive transducer installed on a pipe (Kim *et al.* (2011)) and a magnetostrictive transducer designed to generate frequency-tuned helically propagating shear-horizontal waves (Kim *et al.* (2012)).

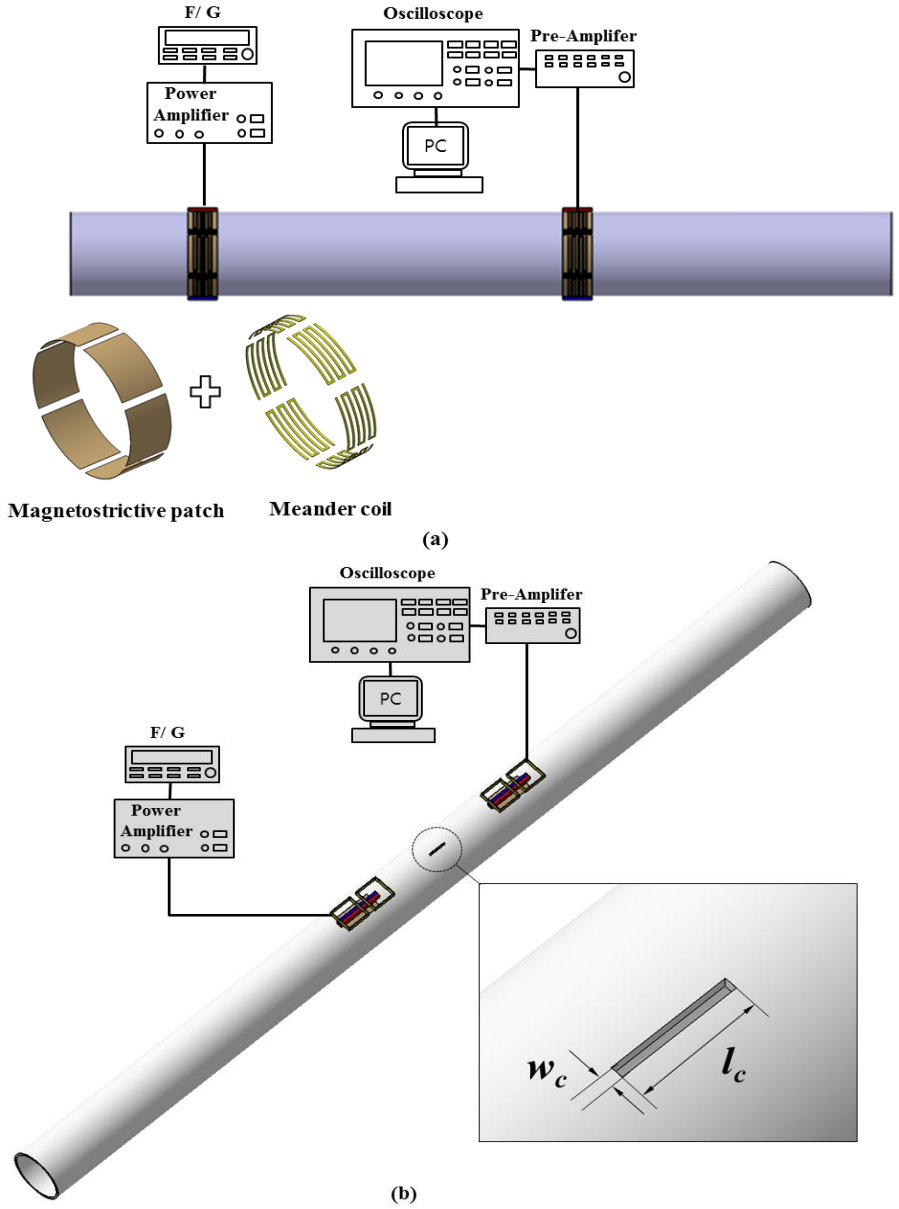

Figure 5.2 Experimental setup used (a) for segmented patch array transducer and (b) for axial crack detection.

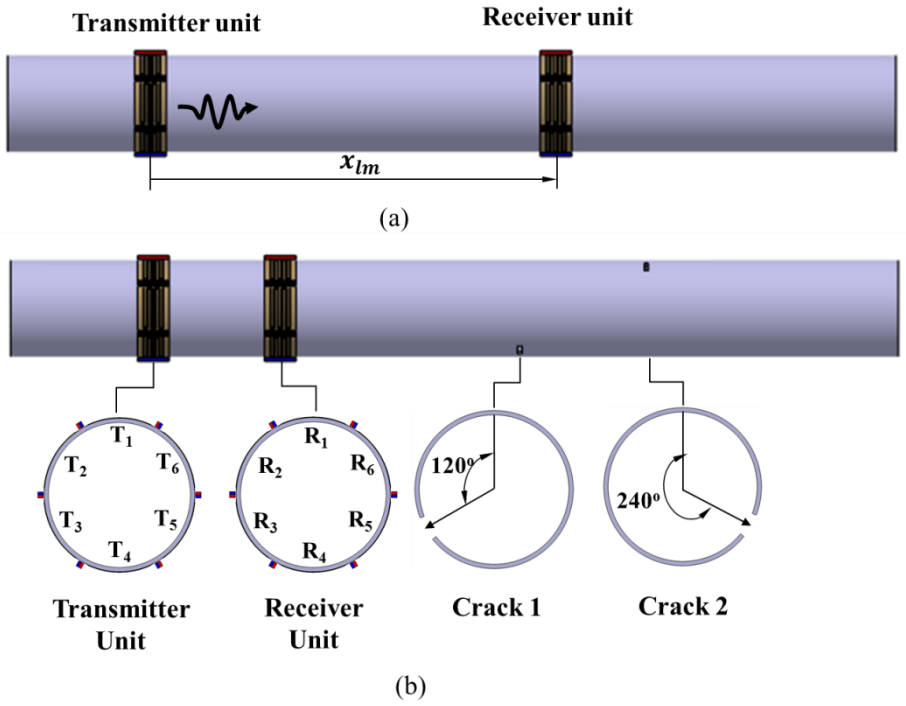

Figure 5.3 Experimental setup for (a) angular profile measurement and (b) damage detection.

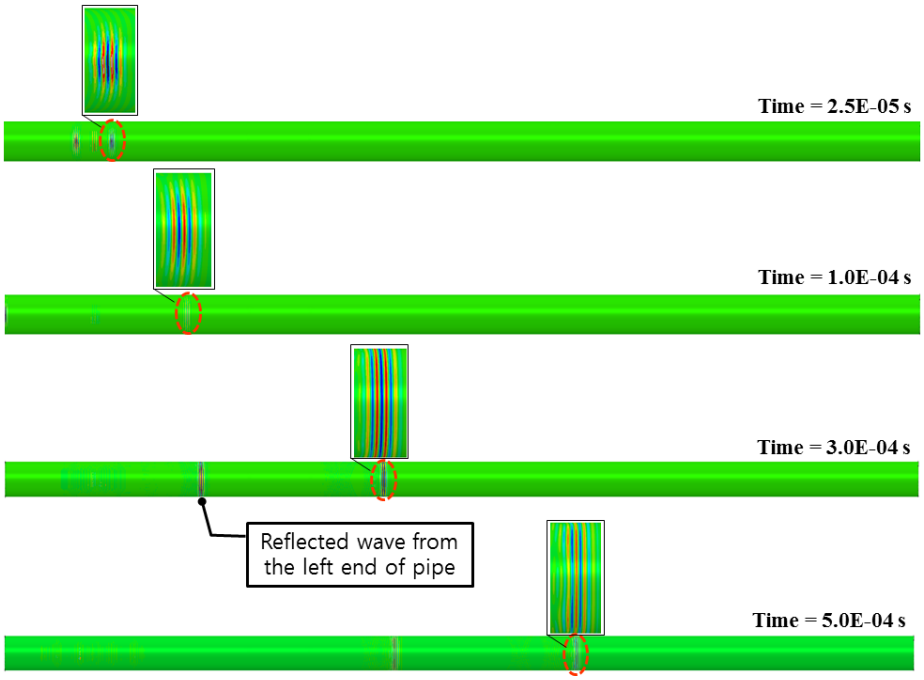

Figure 5.4 The propagation of transient SH_0 waves in segmented-patch-array magnetostrictive transducer at 500 kHz.

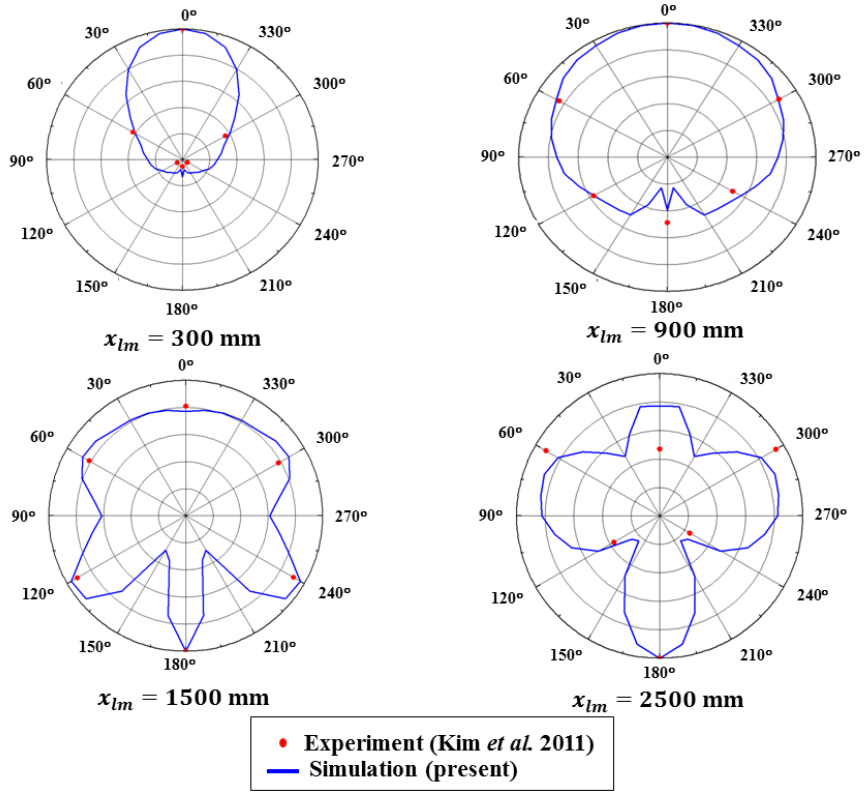

Figure 5.5 Angular profiles of the radiated wave at 500 kHz found at the axial distances of x_{lm} = 300, 900, 1500 and 2500 mm from the excitation transducer.

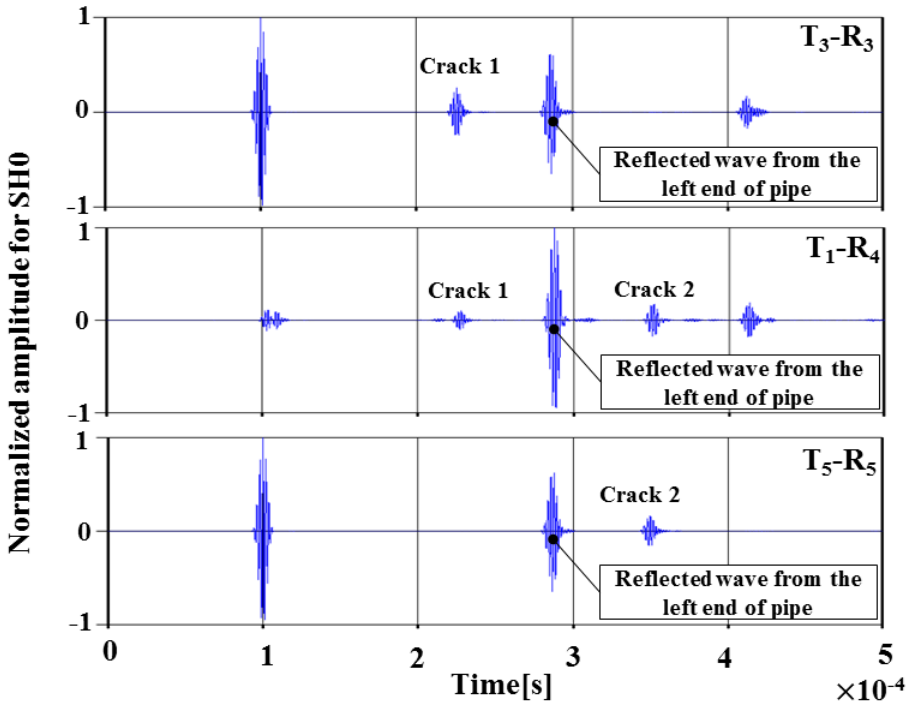

Figure 5.6 The simulated signals by receiver for the $T_3 - R_3$, $T_1 - R_4$, and $T_5 - R_5$ pairs.

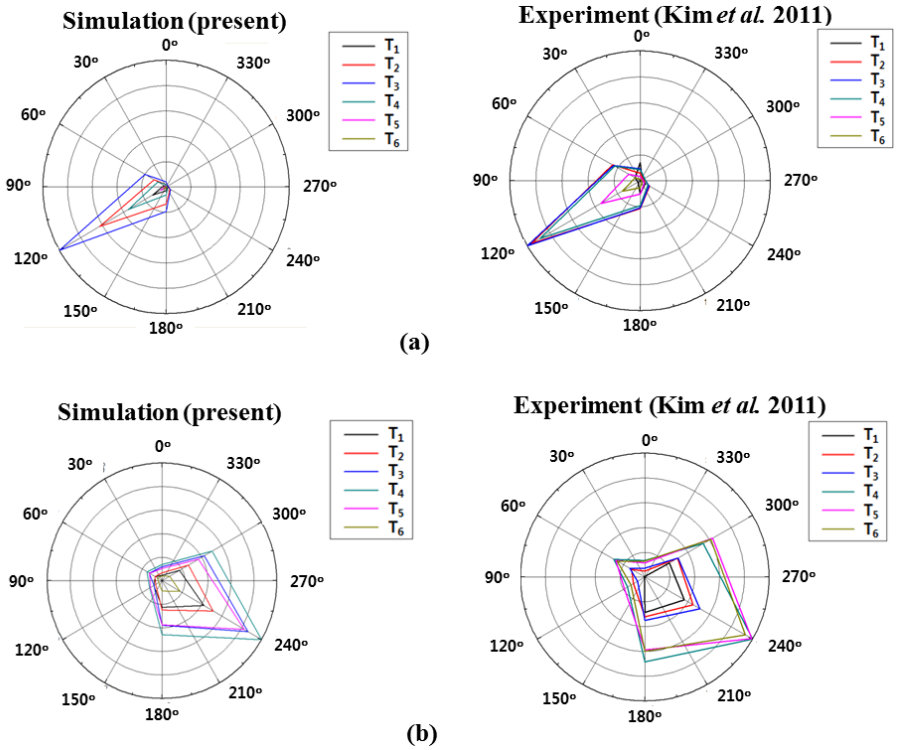

Figure 5.7 The angular distributions of the peak-to-peak values of the reflected waves from (a) crack 1 and (b) crack 2. (Simulation and experimental results are compared.)

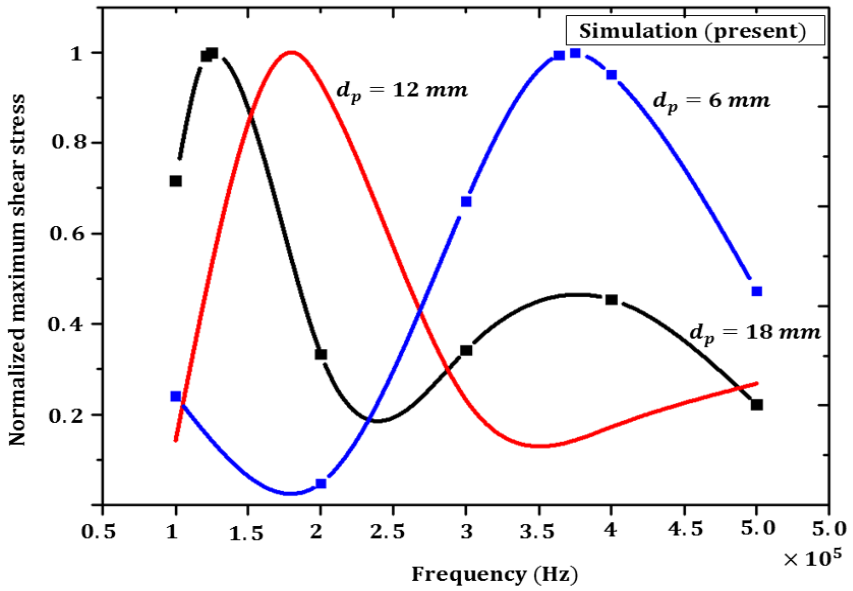

Figure 5.8 The frequency characteristics of the transducer depending on the grating distance d_p. (a) experiment and (b) simulation.

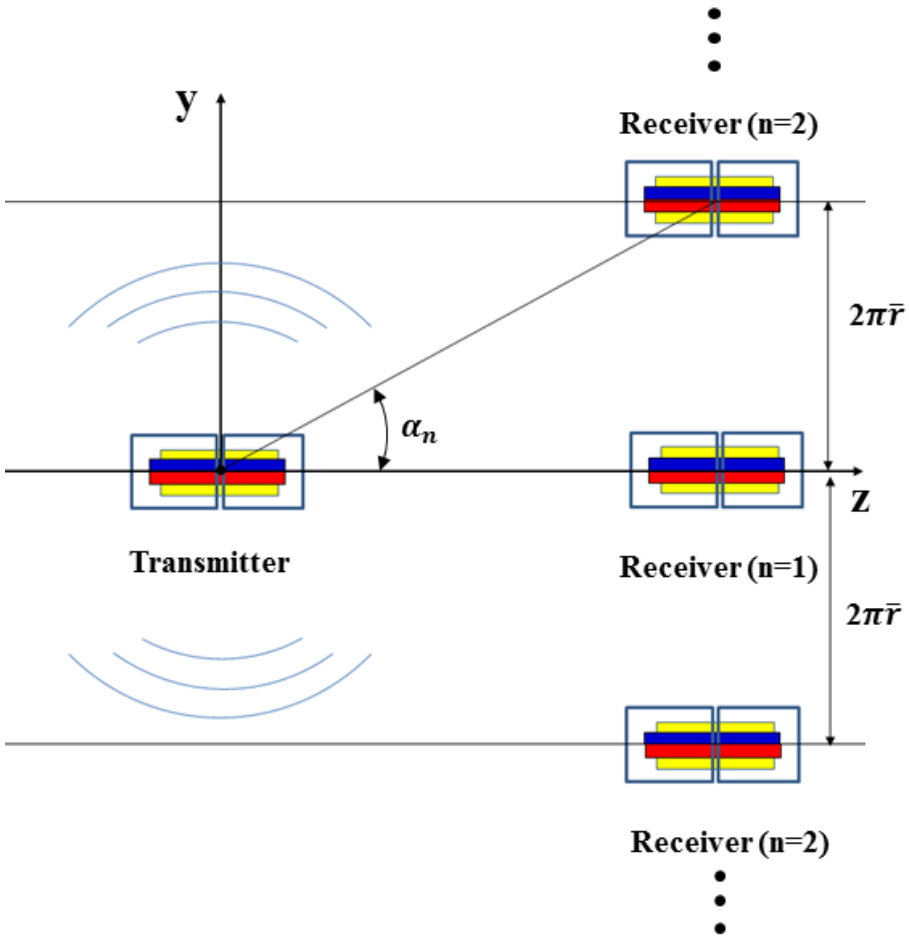

Figure 5.9 (a) Experimental setup in a brass plate (thickness = 1.05mm) to investigate the radiation of the generated wave by the proposed transducer.

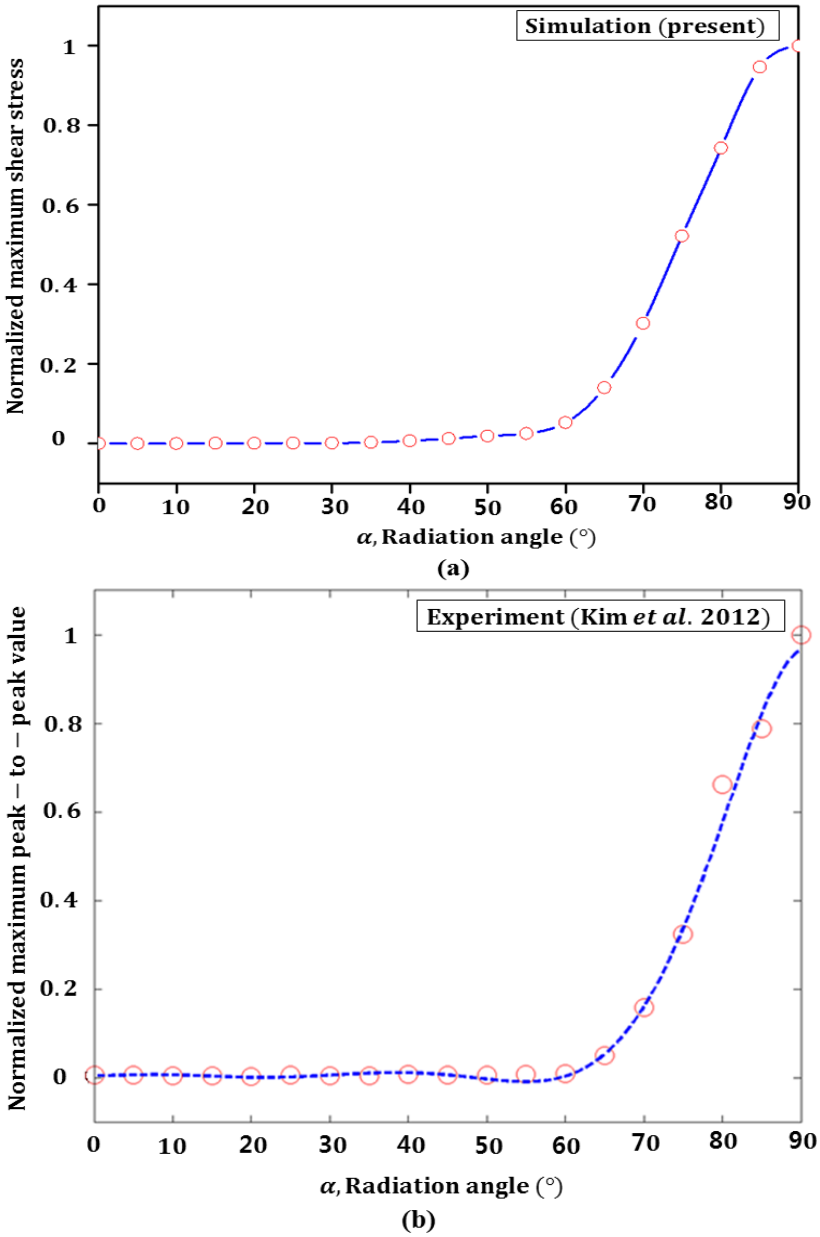

Figure 5.10 The radiation pattern of generated wave by the proposed transducer at 375 kHz.

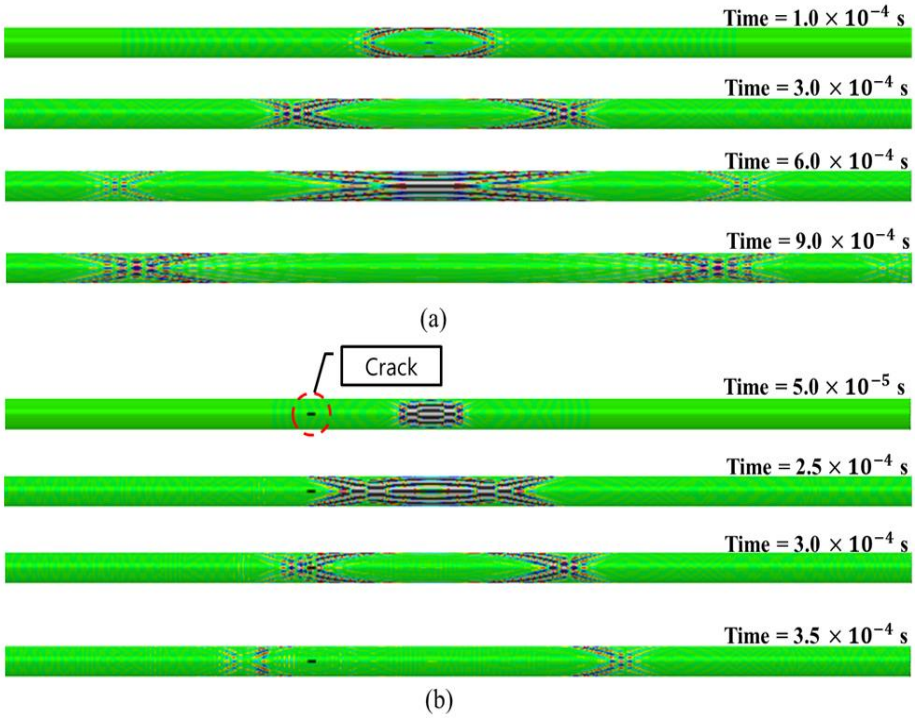

Figure 5.11 Snapshots of stress ($\sigma_{\theta z}$) distribution in (a) undamaged and (b) damaged pipes.

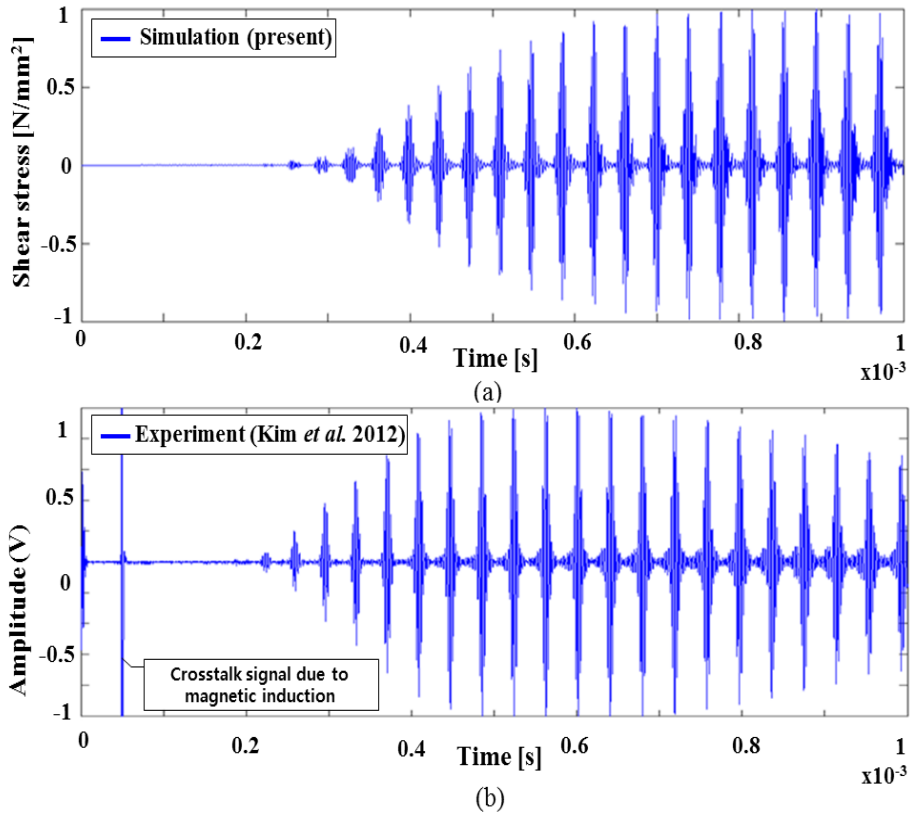

Figure 5.12 (a) The simulated and (b) experimentally measured signals at 375 kHz in an un-cracked and healthy pipe.

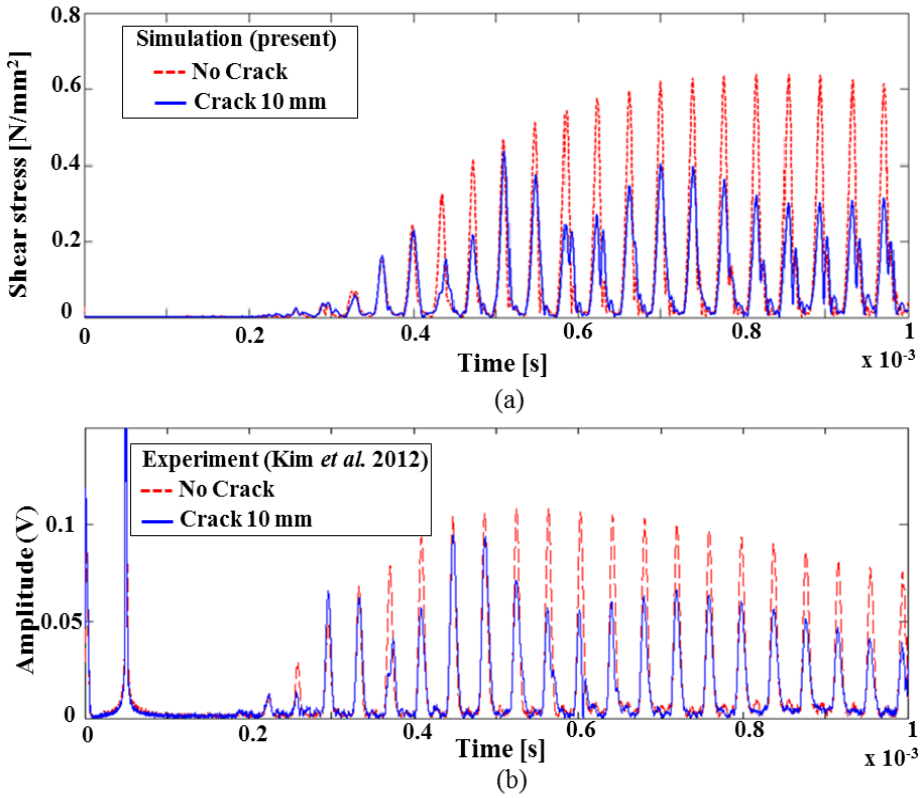

Figure 5.13 (a) The simulated and (b) experimentally measured magnitudes of damaged and undamaged pipes at 375 kHz.

CHAPTER 6

CONCULSIONS

Numerical wave simulations in waveguides excited by various types of magnetostrictive patch transducers were carried out through structural finite element analyses without explicit numerical solutions of the magneto-mechanical coupling wave generation mechanism of the transducer. In our approach, the dynamic deformation of a magnetostrictive patch in the transducer caused by applied time-varying magnetic field, the source of wave excitation in a waveguide, was converted to equivalent distributed forces that are used as the excitation forces for structural finite element analyses. For the force modeling, the magnetostrictive phenomenon was approximated for a patch under both applied time-varying magnetic field and static biasing field. Then, equivalent force models were developed for most of available magnetostrictive patch transducers, such as orientation-adjustable patch-type magnetostrictive transducers (OMPT's), planar-solenoid-array OPMT's for plate applications, segmented-patch-array magnetostrictive transducers and specially-configured magnetostrictive transducers for pipe applications. The structural finite element simulation in waveguides was then conducted by using ABAQUS/Explicit with proper mesh size and time step. The validity of using the proposed force models was confirmed. Wave radiation patterns in waveguides excited by the magnetostrictive patch transducers were calculated by the structural finite element simulation and were shown to agree well with the experimental results. Also, damage estimation of axially-cracked pipes by using helically

propagating shear-horizontal waves was performed by the numerical simulation using the equivalent distributed force models. The resulting simulation results were compared favorably with the experimental results. Considering the simplicity and effectiveness of the proposed equivalent force models, the structural finite element analysis using them can be used as an effective method for design improvement of a wide class of MPT's in the future.

REFERENCES

ABAQUS 2011 Analysis User's Mannual, Version 6.7-1 HKS Inc.

Ajay Raghavan and Carlos E S Cesniv 2005 Finite-dimensional piezoelectric transducer modeling for guided wave based structural health monitoring *Smart Mater. Struct*. 14 1448–1461

Carman G P and Mitrovic M 1995 Nonlinear constitutive relations for magnetostrictive materials with applications to 1-d problems *J. Intell. Mater. Syst. Struct.* 6(5):673-683.

Chen H and Yu W 2014 A multiphysics model for magneto-electro-elastic laminates *Eur. J. Mech. A. Solids* 47 23-44

Cho S H, Lee J S and Kim Y Y 2006 Guided wave transduction experiment using a circular magnetostrictive patch and a figure-of-eight coil in nonferromagnetic plates *Appl. Phys. Lett.* 88 224101

Cho S H, Park C I and Kim Y Y 2005 Effects of the orientation of magnetostrictive nickel strip on torsional wave transduction efficiency of cylindrical waveguides. *Appl. Phys. Lett.* **86**(24)**:** 244101

Choi M S, Kim S Y and Kwun H 2005 An equivalent circuit model of magnetostrictive transducers for guided wave applications *J. Korean Phys. Soc.* 47 454-62

Dapino M J, Smith R C, Faidley L E and Flatau A B 2000 A coupled structural–magnetic strain and stress model for magnetostrictive

transducers *J. Intell. Mater. Syst. Struct.* 11 135-52

Demma A, Cawley P, Lowe M and Roosenbrand AG 2003 The reflection of the fundamental torsional mode from cracks and notches in pipes *J. Acoust. Soc. Am.* 114 611-25

Dhayalan R and Balasubrmaniam K 2010 A hybrid finite element model for simulation of electromagnetic acoustic transducer (EMAT) based plate waves *NDT and E Int.* 43 519-26

Chunhui Yang, Lin Ye, Zhongqing Su and Michael Bannister 2006 Some aspects of numerical simulation for Lamb wave propagation in composite laminates *Composite Structures* 75 267-275.

Engdahl G and Svensson L 1988 Simulation of the magnetosritctive performance of terfenol-d in mechanical devices *J. App. Physics* 63(8):3924-3926.

Gazis DC. 1959 Three-dimensional investigation of the propagation of waves in hollow circular cylinders. I. Analytical foundation. *J. Acoust. Soc. Am.* **31**(5)**:** 568-573

Giurgiutiu V 2003 Lamb wave generation with piezoelectric wafer active sensors for structural health monitoring SPIE Smart Structures Conferences, San Diego

Giurgiutiu V 2007 Structural Health Monitoring with Piezoelectric Wafer Active Sensors (Elsevier Academic Press)

Jiles D C 1995 Theory of the magnetomechanical effect *J. Phys. D:Appl. Phys.* 28 1537-46

Kannan E, Maxfield B W and Balasubramaniam K 2007 SHM of pipes using torsional waves generated by in situ magnetostrictive tapes *Smart Mater. Struct.* 16 2505-15

Kannan K S and Dasgupa A 1997 A nonlinear Galerkin finite-element theory for modeling magnetostrictive smart structures *Smart Mater. Struct.* 6 341-50

Kim H, Jhang K, Shin M and Kim J 2006 A noncontact NDE method using a laser generated focused-Lamb wave with enhanced defect-detection ability and spatial resolution *NDT and E Int.* 39 312-19

Kim H W, Kwon Y E, Cho S H and Kim Y Y 2011 Shear-Horizontal Wave-Based Pipe Damage Inspection by Arrays of Segmented Magnetostrictive Patches *IEEE Trans. Ultrason. Ferroelectr. Freq. Control* 58 2689-98

Kim H W, Lee H J and Kim Y Y 2012 Health monitoring of axially-cracked pipes by using helically propagating shear-horizontal waves *NDT and E Int.* 46 115-21

Kim I K and Kim Y Y 2006 Wireless frequency-tuned generation and measurement of torsional waves using magnetostrictive nickel gratings in cylinders *Sens. Actuators A* **126** 171-8

Kwun H. 2002 Method and apparatus generating and detecting torsional wave inspection of pipes or tubes. U.S. Patent 6429650 B1

Kwun H. 2002 Method and apparatus for nondestructive inspection of plate type ferromagnetic structures using magnetostrictive techniques.

U.S. Patent 6294912 B1

Kwun H and Bartels K A 1998 Magnetostrictive sensor technology and its applications *Ultrasonics* **36** 171-8

Kwun H and Kim S Y 2005 Magnetostrictive sensor for generating and detecting plate guided waves *J. Pressure Vessel Technol.* 127 284-9

Lee H C and Kim Y Y 2002 Wave selection using a magnetomechanical sensor in a solid cylinder *J. Acoust. Soc. Am.* 112 953-60

Lee J S, Cho S H and Kim Y Y 2007 Radiation pattern of Lamb waves generated by a circular magnetostrictive patch transducer *Appl. Phys. Lett.* 90 054102

Lee J S, Kim Y Y and Cho S H 2009 Beam-focused shear-horizontal wave generation in a plate by a circular magnetostrictive patch transducer employing a planar solenoid array *Smart Mater. Struct.* 18 015009

Light GM, Kwun H, Kim S Y and Spinks R L 2001 Method and apparatus for short term inspection or long term structural health monitoring (United states: United States Patent No. 6,396,262 B2)

Lin B and Giurgiutiu V 2006 Modeling and testing of PZT and PVDF piezoelectric wafer active sensors *Smart Mater. Struct.* 15 1085-1093

Liu Z, Zhao J, Wu B, Zhang Y and He C 2010 Configuration optimization of magnetostrictive transducers for longitudinal guided

wave inspection in seven-wire steel strands *NDT and E Int.* 43 484-92

Lowe MJS, Alleyne DN and Cawley P. 1998 Defect detection in pipes using guided waves. *Ultrasonics* **36**(1-5)**:** 147-154

Lu Y, Ye L, Su Z and Yang C 2008 Quantitative assessment of through-thickness crack size based on Lamb wave scattering in aluminum plates *NDT and E Int.* 41 59-68

Murayama R. 1996 Driving mechanism on magnetostrictive type electromagnetic acoustic transducer for symmetrical vertical-mode Lamb wave and for shear horizontal-mode plate wave. *Ultrasonics*. **34**: 729-736

Murayama R. 1999 Study of driving mechanism on electromagnetic acoustic transducer for Lamb wave using magnetostrictive effect and application in drawability evaluation of thin steel sheet. *Ultrasonics*. **37**: 31-38

Murayama R, Makiyama S, Taniguchi. 2004 Development of ultrasonic inspection robot using an electromagnetic acoustic transducer for a Lamb wave and an SH-plate wave. *Ultrasonics*. **42**: 825-829

Ogi H, Goda S and Hirao M 2003 Increase of efficiency of magnetostriction SH-wave EMAT by angled bias field: piezomagnetic theory and measurement *Jpn. J. Appl. Phys.* 42 3020-4

Oh J H, Sun K H and Kim Y Y 2013 Time-harmonic finite element analysis of guided waves generated by magnetostrictive patch

transducers *Smart Mater.Struct.* 22 085007

Park C I, Cho S H and Kim Y Y 2006 Z-shaped magnetostrictive patch for efficient transduction of a torsional wave mode in a cylindrical waveguide *Appl. Phys. Lett.* 89 174103

Perez-Aparicio J L and Sosa H 2004 A continuum three dimensional, fully coupled, dynamic, non-linear finite element formulation for magnetostrictive material *Smart Mater. Struct.* 13 493-502.

Qu J, Berthelot Y and Li Z. 1996 Dispersion of guided circumferential waves in a circular annulus. *Review of Progress in Quantitative NDE, vol. 15*. Plenum, New York, 169-176

Raghavan A and Cesnik CES 2005 Finite-dimensional piezoelectric transducer modeling for guided wave based structural health monitoring *Smart Mater. Struct.* 14 1448–61

Ribichini R, Cegla F, Nagy P B and Cawley P 2010 Quantitative modeling of the transduction of electromagnetic acoustic transducers operating on ferromagnetic media *IEEE Trans. Ultrason. Ferroelectr. Freq. Control* 57 2808-17

Ribichini R, Cegla F, Nagy P B and Cawley P 2010 Study and comparison of different EMAT configurations for SH wave inspection *IEEE Trans. Ultrason. Ferroelectr. Freq. Control* 57 2571-81

Rose J L 1999 Ultrasonic Waves in Solid Media (New York, Cambridge Univ. Press)

Sundaresan M J, Ghoshal A and Schulz M J 2002 A continuous sensor for damage detection in bars *Smart Mater. Struct.* 11 475-88

Sun P, Wu X, Xu J and Li J 2014 Enhancement of the excitation efficiency of the non-contact magnetostrictive sensor for pipe inspection by adjusting the alternating magnetic field axial length *Sensors* 14 1544-63

Thompson R B 1978 Generation of horizontally polarized shear waves in ferromagnetic materials using magnetostrictively coupled meander-coil electromagnetic transducers *Appl. Phys. Lett.* 34 175-7

Thompson R B 1977 Mechanisms of electromagnetic generation and detection of ultrasonic Lamb waves in iron-nickel alloy polycrystals *J. Appl. Phys.* 48 4942-50

Velichko A and Wilcox PD. 2009 Excitation and scattering of guided waves: Relationships between solutions for plates and pipes. *J. Acoust. Soc. Am.* **125**(6)**:** 3623-3631

Yang C, Ye L, Su Z and Bannister M 2006 Some aspects of numerical simulation for Lamb wave propagation in composite laminates *Compos. Struct.* 75 267-75

Yu L, Bottai-Santoni G, Giurgiutiu V 2010 Shear lag solution for tuning ultrasonic piezoelectric wafer active sensors with applications to Lamb wave array imaging *Int. J. Eng. Sci.* 48 848-61

Zhao X and Rose JL. 2004 Guided circumferential shear horizontal waves in an isotropic hollow cylinder. *J. Acoust. Soc. Am.* **115**(5)**:** 1912-1916

국문초록

자기변형 패치 트랜스듀서의 등가 가진 모델을 이용한 유도초음파의 수치해석

김 화 중
서울대학교 대학원
기계항공공학부

자기변형 패치 트랜스듀서는 평판 및 배관 구조물의 유도초음파 탐상에 광범위하게 활용되고 있지만 자기변형 패치 트랜스듀서의 등가가진 모델을 이용한 유한요소 해석에 관한 연구는 매우 제한적이다.

최근, 선형화된 일방향 구조-자기 연성식을 이용한 조화응답해석의 연구 등이 수행되었지만 결함에서 반사되는 반사파에 대한 시간이력에 관한 정확한 정보를 얻기 위해서는 과도응답 해석 수행이 필요하다. 일방향 혹은 양방향 다분야 통합의 과도응답 유한요소 해석은 전기, 자기 및 구조 분야의 물리량이 서로 복잡하게 얽혀있어 긴 해석시간과 많은 컴퓨터 자원을 필요로 한다. 본 연구에서는 응력파 전파에 특화된 상용코드를 활용하여 계산시간을 획기적으로 감소시

킬 수 있는 자기변형 패치 트랜스듀서의 등가가진 모델을 활용한 유한요소 해석 방법을 새롭게 제안하였다. 등가가진 모델을 활용한 유한요소 해석 절차가 정립되면 기존의 상용코드로도 과도응답해석을 수행하여 효율적으로 자기변형패치 트랜스듀서의 유도초음파 탐상 해석을 수행할 수 있다.

본 연구의 핵심내용은 현재 개발되어 사용되고 있는 다양한 종류의 자기변형패치 트랜스듀서의 과도응답해석에서 트랜스듀서를 대체할 수 있는 등가가진 해석모델을 개발하는 것이다. 개발되어진 해석모델의 타당성은 램파 (Rayleigh-Lamb)와 전단파 (Shear-horizontal)의 방사패턴 등 기존에 수행된 실험결과와 비교를 통해 검증하였다.

Keywords: 자기변형 패치 트랜스듀서, 등가 가진모델, 방사 패턴, 과도응답유한요소 해석

Student Number: 2006-30200